CANADIAN THESES ON MICROFICHE

THÈSES CANADIENNES SUR MICROFICHE

National Library of Canada
Collections Development Branch

Canadian Theses on
Microfiche Service

Ottawa, Canada
K1A 0N4

Bibliothèque nationale du Canada
Direction du développement des collections

Service des thèses canadiennes
sur microfiche

NOTICE

The quality of this microfiche is heavily dependent upon the quality of the original thesis submitted for microfilming. Every effort has been made to ensure the highest quality of reproduction possible.

If pages are missing, contact the university which granted the degree.

Some pages may have indistinct print especially if the original pages were typed with a poor typewriter ribbon or if the university sent us an inferior photocopy.

Previously copyrighted materials (journal articles, published tests, etc.) are not filmed.

Reproduction in full or in part of this film is governed by the Canadian Copyright Act, R.S.C. 1970, c. C-30. Please read the authorization forms which accompany this thesis.

AVIS

La qualité de cette microfiche dépend grandement de la qualité de la thèse soumise au microfilmage. Nous avons tout fait pour assurer une qualité supérieure de reproduction.

S'il manque des pages, veuillez communiquer avec l'université qui a conféré le grade.

La qualité d'impression de certaines pages peut laisser à désirer, surtout si les pages originales ont été dactylographiées à l'aide d'un ruban usé ou si l'université nous a fait parvenir une photocopie de qualité inférieure.

Les documents qui font déjà l'objet d'un droit d'auteur (articles de revue, examens publiés, etc.) ne sont pas microfilmés.

La reproduction, même partielle, de ce microfilm est soumise à la Loi canadienne sur le droit d'auteur, SRC 1970, c. C-30. Veuillez prendre connaissance des formules d'autorisation qui accompagnent cette thèse.

THIS DISSERTATION
HAS BEEN MICROFILMED
EXACTLY AS RECEIVED

LA THÈSE A ÉTÉ
MICROFILMÉE TELLE QUE
NOUS L'AVONS REÇUE

Canada

NL 339 (r 85/09)

NAME OF AUTHOR/*NOM DE L'AUTEUR* Marik Dombsky

TITLE OF THESIS/*TITRE DE LA THÈSE* "Energy Dependence of $(p,\pi^- xn)$ Reactions (x = 0 to 7) on Bismuth, From Threshold to 800 MeV"

UNIVERSITY/*UNIVERSITÉ* Simon Fraser University

DEGREE FOR WHICH THESIS WAS PRESENTED/ *GRADE POUR LEQUEL CETTE THÈSE FUT PRÉSENTÉE* M.Sc.

YEAR THIS DEGREE CONFERRED/*ANNÉE D'OBTENTION DE CE GRADE* 1985

NAME OF SUPERVISOR/*NOM DU DIRECTEUR DE THÈSE* J.M. D'Auria, Professor

DATED/*DATÉ* Dec 17/84 SIGNED/*SIGNÉ*

PERMANENT ADDRESS/*RÉSIDENCE FIXÉ* [redacted]

ENERGY DEPENDENCE OF $(p,\pi^- xn)$ REACTIONS (x = 0 TO 7) ON BISMUTH, FROM THRESHOLD TO 800 MeV

by

Marik Dombsky

B.Sc., Simon Fraser University, 1980

A THESIS SUBMITTED IN PARTIAL FULFILLMENT

OF THE REQUIREMENTS FOR THE DEGREE OF

MASTER OF SCIENCE

in the Department

of

Chemistry

SIMON FRASER UNIVERSITY

November, 1984

APPROVAL

Name: Marik Dombsky

Degree: Master of Science

Title of Thesis: Energy Dependence of $(p,\pi^- xn)$ Reactions (x = 0 to 7) on Bismuth, From Threshold to 800 MeV

Examining Committee:

Chairperson: T.N. Bell, Professor

J.M. D'Auria, Senior Supervisor

E.J. Wells

R.G. Korteling

Dr. T. Ruth
Internal Examiner
Research Scientist III
TRIUMF

Date Approved: 29th Nov 1984

PARTIAL COPYRIGHT LICENSE

I hereby grant to Simon Fraser University the right to lend my thesis, project or extended essay (the title of which is shown below) to users of the Simon Fraser University Library, and to make partial or single copies only for such users or in response to a request from the library of any other university, or other educational institution, on its own behalf or for one of its users. I further agree that permission for multiple copying of this work for scholarly purposes may be granted by me or the Dean of Graduate Studies. It is understood that copying or publication of this work for financial gain shall not be allowed without my written permission.

Title of Thesis/Project/Extended Essay

"Energy Dependence of $(p,\pi^- xn)$ Reactions (x = 0 to 7) on ~~Bismuth~~,

From Threshold to 800 MeV"

Author:

(signature)

Marik Dombsky

(name)

Dec 17/84

(date)

ABSTRACT

The energy dependence of the total angle-integrated cross section for the series of reactions $^{209}Bi(p,\pi^-xn)^{210-x}At$, with x = 0 to 7, has been studied from below threshold to 800 MeV at IUCF, TRIUMF and LAMPF, using activation and radiochemical techniques. Excitation functions for the (p,π^-xn) reactions on a heavy target have been measured for the first time by detection of the product nucleus activities. Due to the absence of suitable long-lived astatine isotopes that could be used as tracers for the determination of chemical yields, a technique was developed to determine absolute astatine activities by reference to ^{211}At alpha activity directly radioassayed in thin, irradiated bismuth foils. Modification of existing chemical methods for astatine separation allowed detection of short-lived (≈7 min) isotopes. Since ^{211}At is produced only by secondary (two-step) processes involving reactions of helium fragments produced in the initial proton-target interaction, the detection of ^{211}At activity allows a semi-empirical calculation to be made of the contributions by secondary reactions to the yields of the heavier astatine products. Due to insufficient beam intensities and the interference of secondary reactions, cross sections were not obtained for all products at every proton energy. In particular, the measurement of the coherent (p,π^-) product, ^{210}At, is restricted mainly to upper limits. The mass distributions of the astatine products are consistent with a simple Gaussian shape similar to that observed with (p,xn) reactions on the same target. Extending the Gaussian distribution to astatine isotopes lighter than ^{203}At allows estimation of a mean neutron emission probability and a summed cross section for the total non-charged nucleon exit channel of the inclusive (p,π^-X) reaction. These

estimates are compared to available experimental data on the inclusive reaction and to a simple schematic model that parameterizes the probability of proton emission from the residual nucleus formed in the pion production step. Further comparisons are made with two theoretical calculations of both individual and total (p,π^-xn) excitation functions below 220 MeV proton energy.

for my father

"Alchemy so proceeds that it breaks up a certain body, takes it out of its species, and clothes with the most essential of its components a body of another species. Consequently that alchemical process is best, which proceeds from the selfsame means as nature itself."

- St. Albertus Magnus (1193?-1280)
De Rebus Metalius et Mineralibus

ACKNOWLEDGEMENTS

I would like to thank all of the participants in this series of experiments; specifically, J.L. Clark, I. Kelson, T.J. Ruth, G. Sheffer, T.E. Ward and A.I. Yavin. The guidance and support of my supervisor, J.M. D'Auria, is most gratefully acknowledged. The help of B.J. Dropesky and G. Geisler was instrumental in obtaining the 800 MeV data. I would like to thank C.G. Jones for many elucidating (and sometimes frantic) discussions concerning computers, and L.A. Romines for typing this thesis. Finally, I would like to thank C.J.E. Goozh for putting up with any of this.

TABLE OF CONTENTS

TABLE OF CONTENTS (Cont'd)

LIST OF TABLES

LIST OF TABLES (Cont'd)

LIST OF FIGURES

LIST OF FIGURES (Cont'd)

INTRODUCTION

A Brief Review of (p,π) Experiments

The (p,π) reaction on nuclei has received much attention in recent years[1-5]. Although an extensive body of both experimental and theoretical work has evolved, no clear and simple model of the (p,π) process has yet emerged. In general, most experimental work has involved the measurement of exclusive cross sections, where a specific (usually low-lying) state of an (A+1) nucleus is populated in an A(p,π)A+1 type of reaction. Measurements have usually involved light nuclei, where the states can be easily resolved, and the emission of positive pions, since the cross sections for (p,π^+) are larger than those of the (p,π^-) reaction. However, unexpectedly large cross sections have recently been observed for (p,π^-) transitions to specific two-particle, one-hole states in light and medium weight nuclei[6]. Due to the technical difficulties involved in detecting neutral pions, almost no information is available on the (p,π^0) process.

In heavy nuclei, where states are more closely spaced and cannot be easily resolved, inclusive measurements of the (p,π) process are usually made. Inclusive cross sections measure the total pion production, A(p,π)X, without regard to specific residual products other than the pions. Crawford *et al.*[7] measured the inclusive cross sections for $(p,\pi^\pm)$ on a variety of targets at 585 MeV. On lead, the cross section for (p,π^-) was measured at 41.5 mb, while the (p,π^+) cross section was higher by a factor of two. Cochran *et al.*[8] have measured values of 51.4, 53.7 and 60.4 mb for the (p,π^-) cross section at 735 MeV on ^{181}Ta, ^{208}Pb and ^{232}Th, respectively. Here again, the (p,π^+) cross sections were higher by a factor of two. During the course of the present work, preliminary results became

available for the values of $(p,\pi^{\pm})$ at energies of 330, 400 and 500 MeV. DiGiacomo et al.[9] measured cross sections for π^- production on ^{238}U and obtained values of 5.23, 11.79 and 21.68 mb, respectively, for the three proton energies. These data, when combined with the earlier studies[7,8], provide, for the first time, an energy dependence for the inclusive (p,π) reaction in the medium energy regime.

Two recent determinations of the differential, inclusive $(p,\pi^{\pm})$ cross section at 90° on copper have produced interesting results. Krasnov et al.[10] and Julien et al.[11] studied the energy regions 240-500 MeV and 300-400 MeV, respectively. At 350 MeV, both groups found a narrow resonance (FWHM $\leq$10 MeV) in the energy spectrum of low energy pions. They attribute the enhancement of low energy pion production at E_p = 350 MeV to the formation and subsequent decay of a dibaryon state. The anomaly is also visible in the differential cross section $(d\sigma/d\Omega)$ at 90° as a small deviation from a smooth energy dependence[10].

Both exclusive and inclusive (p,π) measurements employ pion spectrometers (or particle telescopes) to detect the ejected pion rather than the residual nucleus. Radiochemical techniques, while less complex and less expensive than spectrometer measurements, detect only the residual products of a reaction. Due to this technical limitation, cross sections obtained by the study of residuals are averaged over all bound states of the products as well as emission angles and energies of the pions. In spite of this "washing out" of some details of the reaction, information can still be gained from the energy dependence of a formation cross section[12,13]. General features, such as the reaction threshold, the rise or decrease of the cross section and the maximum magnitude, as well as the presence of

peaks or resonances in the excitation function, can serve to distinguish the type of reaction mechanism[12]. Furthermore, if the mass yield distributions of the products are available, some information can be extracted on the energy deposited in the target. Radiochemical measurements have been used extensively, in conjunction with intranuclear cascade model calculations, to deduce the relative importance of nucleon-nucleon and nucleon-pion processes that contribute to an overall end yield of a specific product[13]. Even accepting the limitations of the radiochemical techniques, they can still provide a window on the (p,π) process that is somewhere between the highly selective exclusive measurement and the less selective inclusive measurement.

Radiochemical investigations of (p,π) reactions have included some early studies, such as $^{30}Si(p,\pi^+)^{31}Si$ [14] and $^{65}Cu(p,\pi^-)^{66}Ga$ [15], at energies between 200 and 660 MeV. While these measurements provided crude excitation functions, the data are suspect due to inadequate estimations of contamination by secondary reactions[14]. Later, more thorough investigations studied the $^{65}Cu(p,p\pi^+)^{65}Ni$ [16] and $^{27}Al(p,p\pi^+)^{27}Mg$ [17] reactions to 28 GeV by radiochemical methods. The excitation functions of these reactions are dominated by broad peaks ($\approx$1.3 GeV) attributed to a Δ^{++} resonance. At this time, a measurement of the $^{207}Pb(\alpha,\pi^-)^{211}At$ reaction at 130 MeV is underway at GSI in Darmstadt[18]. This presumably rare reaction channel (representative of "pionic fusion") is being measured by detecting the residual ^{211}At using radiochemical separation.

Recently, two radiochemical measurements of (p,π) reactions on ^{209}Bi have been made. The total reaction cross section for $^{209}Bi(p,\pi^0)^{210}Po$ was measured by a TRIUMF-IUCF collaboration[19], providing an energy-dependent

excitation function for that reaction from threshold to 480 MeV. Calculations using a two-nucleon model gave good agreement with experimental results. Another study, by Clark et al.[20], measured the total cross section for the series of reactions $^{209}Bi(p,\pi^-xn)^{210-x}At$, x = 0-5, at an energy of 200 MeV. The sum of the cross sections for all observed astatine nuclides measured by Clark et al. is 48 ±13 ub and they suggest this amounts to 90-95% of the inclusive (p,π^-) cross section at that energy. While this value is large in comparison to exclusive cross sections, it is two orders of magnitude smaller than the 330 MeV inclusive cross section measured by DiGiacomo et al.[9]. There have been two theoretical attempts to understand the individual and summed cross sections for the $^{209}Bi(p,\pi^-xn)^{210-x}At$ reactions around 200 MeV. Gibbs[21] has calculated individual cross sections for astatine residuals from ^{210}At to ^{203}At. His predicted values agree well with the data at 200 MeV. Long et al.[22], on the other hand, calculated only the summed cross section for all At nuclides. Their calculation is also in good agreement with the 200 MeV data. However, at 220 MeV, the two calculations differ by a factor of two.

The purpose of the present study was to measure the total cross section for the series of reactions $^{209}Bi(p,\pi^-xn)^{210-x}At$, from threshold (≈139 MeV) to as high a proton energy as could be obtained, for as many $^{210-x}At$ products as could be detected. This measurement would provide, for the first time, an energy dependence for the (p,π^-) cross section to all bound states of the residual nuclei. Furthermore, the excitation function for the coherent reaction, $^{209}Bi(p,\pi^-)^{210}At$, could be compared to that of the previously measured $^{209}Bi(p,\pi^0)^{210}Po$ [19]. Of interest is the fact that the (p,π^0) reaction can result from a one-step process (in which the

π^0 is emitted by either the incoming proton or a target nucleon), while the (p,π^-) process requires the interaction of at least one target neutron and, as such, must involve at least two steps. Similar or different shapes for the (p,π^-) and (p,π^0) excitation functions can be expected to reflect similar or different underlying reaction mechanisms. Further comparisons could be made with the two theoretical calculations[21,22] for both individual and summed cross sections, as well as to the inclusive cross section measurements at higher energies[7-9]. The calculation of Long et al.[22] is based on a series of nucleon-nucleon reactions, while that of Gibbs[21] involves a coherent interaction leading to typical shell model states. Comparison of the experimental (p,π^-xn) cross sections to the two theoretical predictions can give an indication of which mechanism best describes the reaction channel. The (p,π^-xn) reaction channels must be some subset of the greater (p,π^-X) inclusive reaction. Summing over all values of x would provide a measure of the magnitude of the non-charged nucleon emission component of the (p,π^-X) reaction. Finally, the distribution of residual astatine nuclides can provide a measure of the most likely number of neutrons to be evaporated. This can provide some information on the role the nucleus plays in (p,π^-) reaction. Specifically, the average number of evaporated neutrons allows the estimation of the average excitation energy of the residual nucleus as well as the momentum transfer to the nucleus. An estimate of the average momentum transfer is of interest since (p,π) reactions are typified by a large momentum mismatch caused by the mass differences of the incident proton and final pion.

Bismuth was chosen as a target for practical reasons. The body of experimental data and theoretical calculations already available for

comparison with the present measurements has been mentioned previously. As well, bismuth is monoisotopic (^{209}Bi is the only stable nuclide), allowing high purity targets to be constructed. These targets can be fashioned into very thin foils, thus decreasing the probability of secondary reactions. Furthermore, the (p,π^-xn) products from a bismuth target are astatine nuclides that can be purified by existing chemical techniques. About half of the astatine nuclides are alpha emitters that can be counted with high sensitivity in low amounts with essentially no background interference.

Principles of the Experiment

As with most experiments, the principles of the present experiment are simple; the difficulty only arises in the execution. In order to measure the (p,π^-xn) cross sections, ^{209}Bi targets were irradiated by sufficiently intense beams of monoenergetic protons. The targets then underwent chemical manipulation that extracted the astatine nuclides produced in the targets. The decays of the radioactive astatines were observed by their characteristic alpha and gamma emissions and the cross sections for production were calculated.

In order to obtain proton energies from the threshold for the (p,π^-) reaction ($\approx$139 MeV) to 800 MeV, experiments were conducted at three accelerator facilities: IUCF, TRIUMF and LAMPF. While TRIUMF and LAMPF beams were intense enough for detection of all astatine products, the low intensity beam at IUCF allowed detection of only ^{211}At, ^{209}At and ^{207}At.

The presence of ^{211}At in the irradiated targets provided both problems and solutions for the experiment. ^{211}At cannot be produced in the (p,π^-) process on ^{209}Bi but results only from secondary reactions in the target. These reactions involve the emission of an alpha or ^{3}He particle in an

interaction between an incoming proton and a target nucleus. The alpha (or ^{3}He) then reacts with a second target nucleus to produce an astatine nucleus:

$$^{209}Bi(p,\alpha)X$$
$$\downarrow$$
$$^{209}Bi(\alpha,xn)^{213-x}At$$

Though secondary reactions are target thickness-dependent and can be minimized by using thin targets, their magnitude is such as to be of the same order as that of the $(p,\pi^{-}xn)$ reactions, even in thin targets. Therefore, secondary production of astatine poses a serious contamination problem. To separate the $(p,\pi^{-}xn)$ cross sections from the total astatine production cross sections (due to both primary and secondary reactions), calculations were performed to estimate the secondary contributions from known (p,α) and (α,xn) cross sections. These calculations are detailed in a separate section of this thesis.

While the presence of ^{211}At presented a problem in regard to secondary reactions, it provided a solution with respect to chemical separation efficiency calculations. Since astatine has no long-lived isotopes that can be conveniently used as tracers for the determination of chemical separation efficiency, a method was developed which enabled the determination of cross sections without reference to chemical yield. Two thin bismuth targets of equivalent thickness were irradiated at each proton energy. The first target was directly radioassayed for a distinct high energy alpha activity due to ^{211}Po, which is in secular equilibrium with its parent, ^{211}At. The production cross section for ^{211}At at that specific energy and target thickness was then calculated. The second target underwent

immediate chemical separation and counting for astatine nuclides. All cross sections calculated from the separated activities were expressed as ratios with respect to ^{211}At activity. The absolute cross section for a particular astatine nuclide could then be calculated from the product of the absolute ^{211}At cross section and the cross section ratio:

$$\sigma_x = \underbrace{\sigma_{^{211}At}}_{\text{from Target \#1}} \times \underbrace{\frac{\sigma_x}{\sigma_{^{211}At}}}_{\text{from Target \#2}}$$

EXPERIMENTAL

Proton Irradiation Procedures

Proton irradiations of bismuth targets were performed at three accelerator facilities. Proton energies of 120, 160, 180, 200 and 214 MeV were obtained at the Indiana University Cyclotron Facility (IUCF) in Bloomington, Indiana. Energies of 188, 210, 225, 252, 300, 350, 399, 450 and 481 MeV were used at the Tri-University Meson Facility (TRIUMF) in Vancouver, B.C. Multiple irradiations at a proton energy of 800 MeV were performed at the Clinton P. Anderson Meson Physics Facility (LAMPF) in Los Alamos, New Mexico. High-purity bismuth targets, with a quoted error in thickness of $\lesssim 6\%$, were prepared by the staff of the IUCF target shop and were used for irradiations at all three facilities. Thin targets consisted of 1-2 mg/cm^2 of bismuth, evaporated onto a 4.1 mg/cm^2 aluminum backing. Thicker targets ($\approx$30-100 mg/cm^2), used only at IUCF, were free-standing bismuth foils. Some very thick targets (1 g/cm^2) of Bi_2O_3 were used at IUCF to study secondary reactions.

At IUCF, targets were irradiated under vacuum in the isotope production beamline. The TRIUMF irradiations were also conducted in vacuum in the SFU gas jet target cell on beamline 4A. At LAMPF, targets were irradiated at two target stations. The first employed the nuclear chemistry pneumatic rabbit system in experimental area B to insert the targets into the beam. The second station was in the isotope production cave in area A and required manual insertion and removal of targets. Both target stations were in air.

Beam Integration

Proton beam integration at IUCF was measured using a Faraday cup downstream from the target, while at TRIUMF and LAMPF it was deduced from ^{24}Na activity produced in 1.85 mg/cm^2 aluminum monitor foils backing the target. The ^{24}Na is produced by the ^{27}Al(p,3pn)^{24}Na reaction. The cross section for this reaction has been determined to 1 GeV for the purpose of monitoring proton flux during irradiation[23]. For each proton energy, three aluminum foils of the same dimensions as the target were irradiated immediately downstream of the target. Recoil losses of ^{24}Na were avoided by measuring the activity of the middle foil in the stack[24]. At TRIUMF, where the beam spot is well defined ($\lesssim$3 mm diameter), the target and monitor stack was a 1 inch-square. At LAMPF, the proton beam was much larger and irregular in shape. In order to provide targets for direct counting, the LAMPF target stacks consisted of 12 mm diameter circular discs. These discs were entirely covered by the much larger beam spot and provided sources of the same geometry as the chemically-separated samples. Targets that underwent chemical separation were 1 inch-squares.

The ^{24}Na activity in the monitors ($t_{1/2}$ = 15.03 h)[25] was counted periodically for several days after bombardment. At TRIUMF, the ^{24}Na was monitored by detection of its 1368.53 keV gamma radiation (100% branching ratio), using a Ge(Li) detector. At LAMPF, a NaI detector, specifically calibrated for ^{24}Na β^- radiation was used. Decay curves were analysed using least squares methods; the SFU program, LSL, on an IBM 4341 and the LAMPF CLSQ program on a PDP-11/34. While both detection techniques gave acceptable results, of comparable accuracy, the β^- decay curves contained a longer-living ($t_{1/2}$ >15 h) component that could not be resolved. Proton

flux was calculated using the formula:

$$\Phi = \frac{A_{EOB}}{N \cdot \sigma 24_{Na} \cdot (1-e^{-\lambda t_B})} \qquad (1)$$

where $A_{EOB} \equiv$ absolute ^{24}Na activity at end of bombardment (d/s);

$N \equiv$ aluminum target thickness (nuclei/cm^2);

$\sigma 24_{Na} \equiv$ cross section for the $^{27}Al(p,3pn)^{24}Na$ reaction (cm^2);

$\lambda \equiv$ decay constant for ^{24}Na;

$t_B \equiv$ bombardment time;

$\Phi \equiv$ proton flux (protons/sec).

Particulars of the proton flux calculations for irradiations at the three facilities are given in Tables I, II and III.

Beam currents were periodically monitored during the target bombardments to insure that flux variations were not a cause of additional uncertainties. In general, beam currents were steady at all three facilities, with only a few interruptions. Beam "on-off" periods were noted and saturation factor corrections calculated for the 399 MeV TRIUMF run and five of the thirteen LAMPF runs. The corrections were on the order of 4-9% of the final cross section values for ^{24}Na and the various At nuclides. The greatest correction was for the At-10 run at 800 MeV where the beam was off for 13% of the total irradiation period. This resulted in a calculated correction of 15% to the final ^{211}At cross section.

Direct Target Counting

The ^{211}At ($t_{1/2}$ = 7.21 h) produced by secondary reactions of helium fragments in the bismuth targets decays by alpha emission to ^{207}Bi (41.9%)

Table I

IUCF Proton Flux Summary

E_p[a] (MeV)	Φ (p/sec)	Average Beam Current (nA)	t_B (h)
120_{104}	1.80×10^{12}	288	2.18
120_{1000}	1.41×10^{12}	226	2.50
160	3.77×10^{12}	604	3.05
180	4.48×10^{11}	72	4.58
200	2.99×10^{12}	479	5.33
214	1.32×10^{11}	21	2.53

[a] Subscripts on the two 120 MeV runs refer to target thicknesses in mg/cm^2.

Table II

TRIUMF Proton Flux Summary

E_p (MeV)	$\sigma_{^{24}Na}$[a] ($\times 10^{-27}$ cm^2)	t_B[b] (h)	A_{EOB} (^{24}Na-γ) ($\times 10^5$ d/sec)	Φ ($\times 10^{13}$ p/sec)	Average Current (μA)
188	9.3	0.55	2.05 ±0.08	2.1 ±0.2	3.4
210	9.3	0.32	2.15 ±0.06	3.9 ±0.3	6.2
225	9.4	0.50	2.26 ±0.18	2.6 ±0.3	4.1
252	9.5	0.43	2.24 ±0.15	2.9 ±0.3	4.6
300-1	10.1	0.50	2.09 ±0.10	2.2 ±0.2	3.5
300-2	10.1	0.50	1.15 ±0.08	1.2 ±0.1	1.9
350	10.3	0.53	1.11 ±0.03	1.0 ±0.1	1.6
399	10.5	0.41	0.92 ±0.01	1.2 ±0.1	1.8
450	10.5	0.60	1.04 ±0.02	0.88 ±0.1	1.4
481	10.5	0.59	2.38 ±0.06	2.0 ±0.1	3.3

[a] ±6.5% uncertainty, from Reference 23.

[b] ±1.7% estimated average uncertainty.

Table III

LAMPF 800 MeV Proton Flux Summary

Target	t_B (h)	Φ[a] ($\times 10^{11}$ p/sec)
At-2	0.17	8.0 ±0.8
At-3	0.37	21.5 ±2.3
At-6	1.17	56.7 ±6.2
At-7d	1.00	57.2 ±5.8
At-10d	1.00	20.3 ±2.2
At-11	0.88	51.5 ±5.5
At-12	0.97	39.8 ±4.2

[a] Flux values were calculated by Dr. J.L. Clark, using the LAMPF CLSQ program on the CNC-11 PDP-11/34. The cross section for ^{24}Na production in ^{27}Al by 800 MeV protons was taken to be 10.1 ±1.0 mb[23].

and by electron capture to ^{211}Po (58.1%). The ^{211}Po daughter decays almost immediately ($t_{1/2}$ = 0.525 sec) by emission of an alpha particle, accounting for 57.2% of the parent ^{211}At decays. The energy of this ^{211}Po alpha (7.45 MeV) is much higher than the energies of alphas emitted by other reaction products ($\lesssim$6 MeV). This clear energy separation of an alpha, characteristic of ^{211}At, allows direct detection of ^{211}At in a thin, irradiated target without reliance on chemical separation techniques.

The 7.45 MeV alpha energy is also sufficiently high to prevent absorption of the alpha in the target itself if the target is sufficiently thin. To test absorption of alphas in thin bismuth layers, a 1.94 $\pm$0.12 mg/cm^2, free-standing bismuth target was placed over a commercial ^{241}Am alpha source. Alpha counts, 30 min in duration, using a silicon surface barrier detector, showed that, while the ^{241}Am alpha peaks were greatly broadened and slightly shifted to lower energy, no net loss of alpha activity could be detected between counts of the bare source and counts of the source covered by the bismuth target. Since the ^{241}Am alpha energies (5.485, 5.742 MeV[25]) are less than the ^{211}At alpha energy and targets used for direct counting were $\leq$2.0 mg/cm^2 of bismuth, no absorption corrections were required for the direct target counts.

At TRIUMF, targets that were to be direct counted were irradiated for average periods of $\approx$30 min. The targets were then removed from the beam while targets for chemical separation were irradiated. After a period of 2-3 h, short-lived activities in the targets had decayed sufficiently to allow the targets to be counted. The targets were counted in a vacuum chamber, using a silicon surface barrier detector. The solid angle subtended by the detector was determined using a standard ^{241}Am source of

approximately the same diameter as the beam spot. Overall detection efficiency at a source-detector separation of 1.5 cm was 5.35 ±0.27%. Particulars of the direct target counts are shown in Table IV.

The direct target counting at LAMPF was essentially the same as at TRIUMF. However, as previously noted, the large beam spot produced disc sources rather than point sources. This required the alpha detector to be calibrated for sources of relatively large diameter. A ^{210}Po alpha source was prepared using commercially-purchased ^{210}Po. This source had the same dimensions as the direct counting targets and was used to calibrate the surface barrier detectors. The higher activities of the LAMPF targets allowed several successive counts to be measured in some cases. When this was possible, decay curves were analysed by least squares fits. Counting details for the LAMPF direct targets are summarized in Table V.

Though an attempt was made to directly count thin targets at IUCF, the low beam currents prevented the direct counting technique from being used at that facility. Thick targets irradiated at IUCF underwent chemical separation for astatine. The chemical efficiencies of the separations were determined by Dr. T.E. Ward, of IUCF, by calibration of the extraction columns used at IUCF. The Indiana data analysis was performed by Dr. Ward and the final cross section values are quoted in the Results section. The quoted errors include uncertainties in half lives, branching ratios, detection efficiencies, chemical separation efficiencies and beam integration.

Chemical Separation of Astatine

Astatine is separated from bismuth targets by either solvent extraction or distillation methods[18,26-30]. The solvent extraction methods generally require the dissolution of the target in nitric acid, after which

Table IV

Summary of TRIUMF Direct Target Counts

E_p (MeV)	Target Thickness (mg/cm^2)	t_B (h)	Count Duration (h)	Dead Time (%)	^{211}At Counts	^{211}At Activity[a] at EOB (d/sec ±0.01)
188	1.01	0.55	1.49	5.3	491	0.13
210	0.94	0.32	1.24	6.5	407	0.11
225	1.10	0.50	2.78	5.0	978	0.13
252	1.13	0.43	1.84	3.8	752	0.17
300-1	1.14	0.50	2.78	1.5	495	0.12
300-2	0.94	0.50	3.10	1.9	607	0.08
350	1.18	0.53	1.70	2.8	587	0.13
399	0.84	0.41	2.35	1.6	407	0.07
450	1.04	0.60	3.08	1.9	699	0.09
481	0.77	0.59	0.90	5.1	530	0.21

[a] Corrected for dead time, decay time, branching ratios and detector solid angle.

Table V

Summary of LAMPF Direct Target Counts

Target	Target Thickness (mg/cm^2)	t_B (h)	Count Duration (h)	Time After EOB (h)	^{211}At Counts	^{211}At Activity[a] at EOB (d/sec)
At-2	1.76	0.17	1.00	.28	119	0.55 ±0.05
At-3	2.00	0.37	0.12	0.22	129	4.46 ±0.57
"	"	"	0.50	0.39	442	
At-6	1.07	1.17	0.50	1.54	1798	18.40 ±0.12
"	"	"	0.28	5.12	710	
At-7d	0.56	1.00	0.28	1.92	411	8.24 ±0.46
"	"	"	0.56	3.79	757	
"	"	"	0.28	6.77	272	
At-10d	0.34	1.00	6.67	18.35	701	2.17 ±0.16
At-11	0.69	0.88	11.04	9.93	867	0.83 ±0.06
At-12	0.71	0.97	0.97	8.85	1080	6.82 ±0.47

[a] Corrected for dead time, decay time, branching ratios and detector solid angle.

the astatine (presumably in the zero valence state, At^0) is extracted into an organic phase consisting of benzene, carbon tetrachloride, di-isopropyl ether or another solvent[26-30]. The astatine is then reduced to the astatide ion (At^-) by a suitable reducing agent (Sn^{2+} in acid, SnO_2^{2-} in base or Zn in H_2SO_4) and separated from solution by coprecipitation with insoluble iodides of silver, palladium, thalium or lead, or with tellurium metal. The astatide can also be removed from solution at this point by spontaneous plating onto silver or platinum surfaces[26]. While plating astatine onto a silver foil provides an attractive method of making a thin, stable source for alpha counting, the solvent extraction methods have major drawbacks. One of the difficulties is that the time required for an extraction-back extraction type of separation, added onto the plating time, makes the method too lengthy for detection of short-lived astatines. The other drawback is that polonium is extracted by similar techniques. Since polonium daughters of some astatine nuclides were intended to be counted, the solvent extraction methods were not used.

The distillation methods of astatine extraction[18,30] require melting the target (≈270°C) in vacuum or an inert gas. The astatine is then deposited directly onto a cooled metal foil above the melt, or frozen out in a U-tube for use in solution. The distillation methods suffer from the same drawbacks as the solvent extraction methods; distillation requires time and, at high temperatures, polonium begins to distill along with the astatine. Distillation was not used to extract astatine for the present work.

The separation method employed in the current study was based on an elegant technique first described by Bochvarova et al.[31]. The method

relies on the well-documented, quantitative coprecipitation of astatine ions with tellurium metal[26]. However, rather than precipitating the astatine with tellurium, the tellurium metal is used as packing in an ion exchange column. The target is dissolved and the astatine reduced. The solution is then passed through the tellurium column, separating it from most of the radionuclides initially present in the target. The astatine absorbed on the column is eluted by a solution containing hydroxide ion, leaving polonium still absorbed on the column. Bochvarova et al.[31] explain the coordination of At^- to Te in terms of Lewis acid-base properties. The terminal tellurium atoms in the crystals of the column packing act as electron pair acceptors due to their $5s^2 5p^4$ electron configuration. The astatide ions, with a $6s^2 6p^6$ configuration, donate an electron pair to form a coordinate bond. The hydroxyl ion, with three electron pairs and a high tendency to form coordinate bonds, presumably displaces the more polarizable astatide ion from the tellurium.

This separation technique has been modified and extensively studied by Ruth[32] and Clark[33]. The specific separation scheme used in the present work was as follows. Crystalline tellurium metal was crushed and sifted to obtain fresh column packing with a size of ≈30 mesh. Columns, 10 cm long, with a 0.5 cm diameter, were obtained by packing the tellurium into disposable pasture pipettes. The columns were stored in dilute solutions of hydrochloric acid. Holding reservoirs were constructed by attaching 10 mL transfer pipettes to the columns. Figure 1a shows a typical exchange column apparatus. Prior to use, the columns were washed with solutions of 1 M SnCl in 8 M HCl, H_2O, 2 M NaOH, H_2O and 8 M HCl. This washing procedure seems to remove traces of impurities in the tellurium that interfere

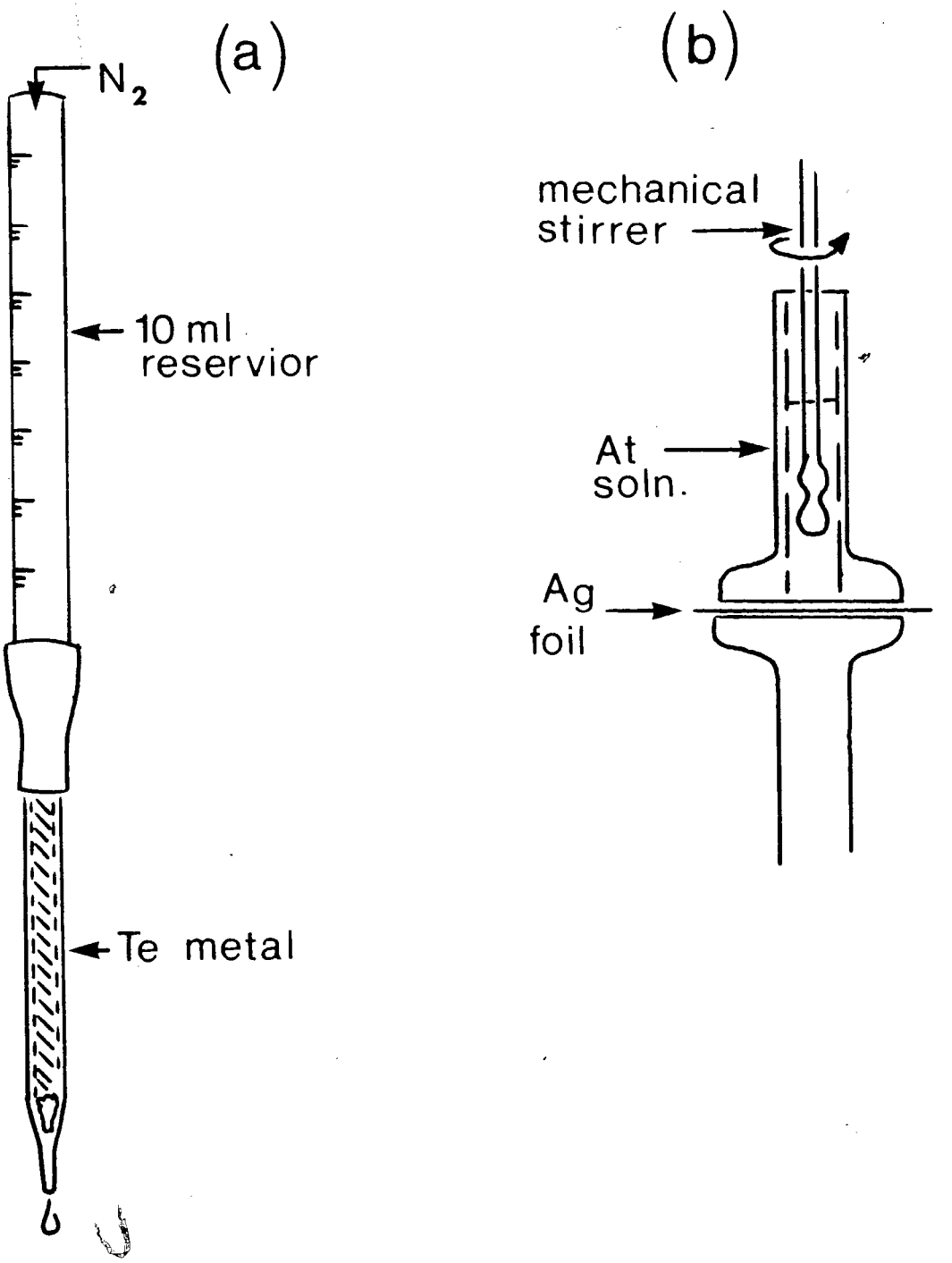

Figure 1 Chemical Separation Apparatus

a: Tellurium Column

b: Plating Cell

in later plating of At^- onto silver. Immediately after irradiation, the bismuth targets were dissolved with a minimum of conc. HNO_3. Excess nitrates were neutralized by dropwise addition of a 10% $NH_2OH \cdot Cl$ solution. This target solution was then acidified to 8 M in HCl and the At^0 reduced by addition of 1 M $SnCl_2$ in 8 M HCl. The solution (about 10-15 mL volume at this point) was loaded onto the tellurium column. The solution was forced through the column at a rate of ≈10 mL/min by a stream of nitrogen. The column was then quickly washed with rinses of 8 M HCl and water (≈30 mL of each). Finally, about 2 mL of 2 M NaOH was used to elute the At^- from the column at a rate of ≈2 mL/min. The separated solution was acidified to 1.5 M in HCl and the astatine plated onto a silver foil. The plating apparatus consisted of a 1 cm diameter filter chimney held onto a freshly-cleaned silver foil (rinsed in 6 M HNO_3 and H_2O). Plating times were on the order of 15 min, during which time the solution was mechanically stirred. Figure 1b displays a typical plating apparatus. The final 1 cm diameter astatine source was dried with methanol and immediately counted. The time from end of bombardment to first count was typically on the order of 30-40 min.

To ensure that no contamination of astatine or polonium was transferred from one separation to another, all apparatus (columns, plating chimneys and glassware) were used only once. The selectivity of the column technique was examined by comparing the alpha activity in the ^{208}Po energy region of the source alpha spectra to the predicted yields of ^{208}Po, based on known (p,xn) cross sections for the proton energies under consideration[19,34]. Calculations showed that $\leq$0.04% of the polonium passed through the separation. A schematic representation of the chemical

separation is given in Figure 2.

Data Acquisition and Analysis

The counting techniques for direct targets have been previously described. Spectra were collected using a silicon surface barrier detector mounted in fixed geometry in a vacuum chamber. Alpha energy and detection efficiency calibration were accomplished by using a standard ^{241}Am alpha source. All spectra were collected in a multichannel analyzer using 1024 channels. Hard copy outputs of the spectra were analysed by hand, summing the counts in the ≈7.45 MeV alpha energy region. Statistical uncertainties were taken as being the square root of the total counts. A typical direct target spectrum is shown in Figure 3a.

Absolute ^{211}At production cross sections at each proton energy were calculated using the formula:

$$\sigma 211_{At} = \frac{A_{EOB}}{(B.R.)\cdot(D_{eff})\cdot N\cdot\Phi_p\cdot(1-e^{-\lambda t_B})} \qquad (2)$$

where $\sigma 211_{At}$ ≡ total production cross section for ^{211}At for a specific proton energy and target thickness (cm^2);

A_{EOB} ≡ ^{211}At activity at end of bombardment (counts/sec);

B.R. ≡ branching ratio of 7.45 MeV alpha of ^{211}At;

D_{eff} ≡ Detection efficiency for the 7.45 MeV alpha;

N ≡ atomic density of the bismuth target (atoms/cm^2);

Φ_p ≡ proton flux (protons/sec);

λ ≡ decay constant of ^{211}At (h^{-1});

t_B ≡ duration of bombardment (h).

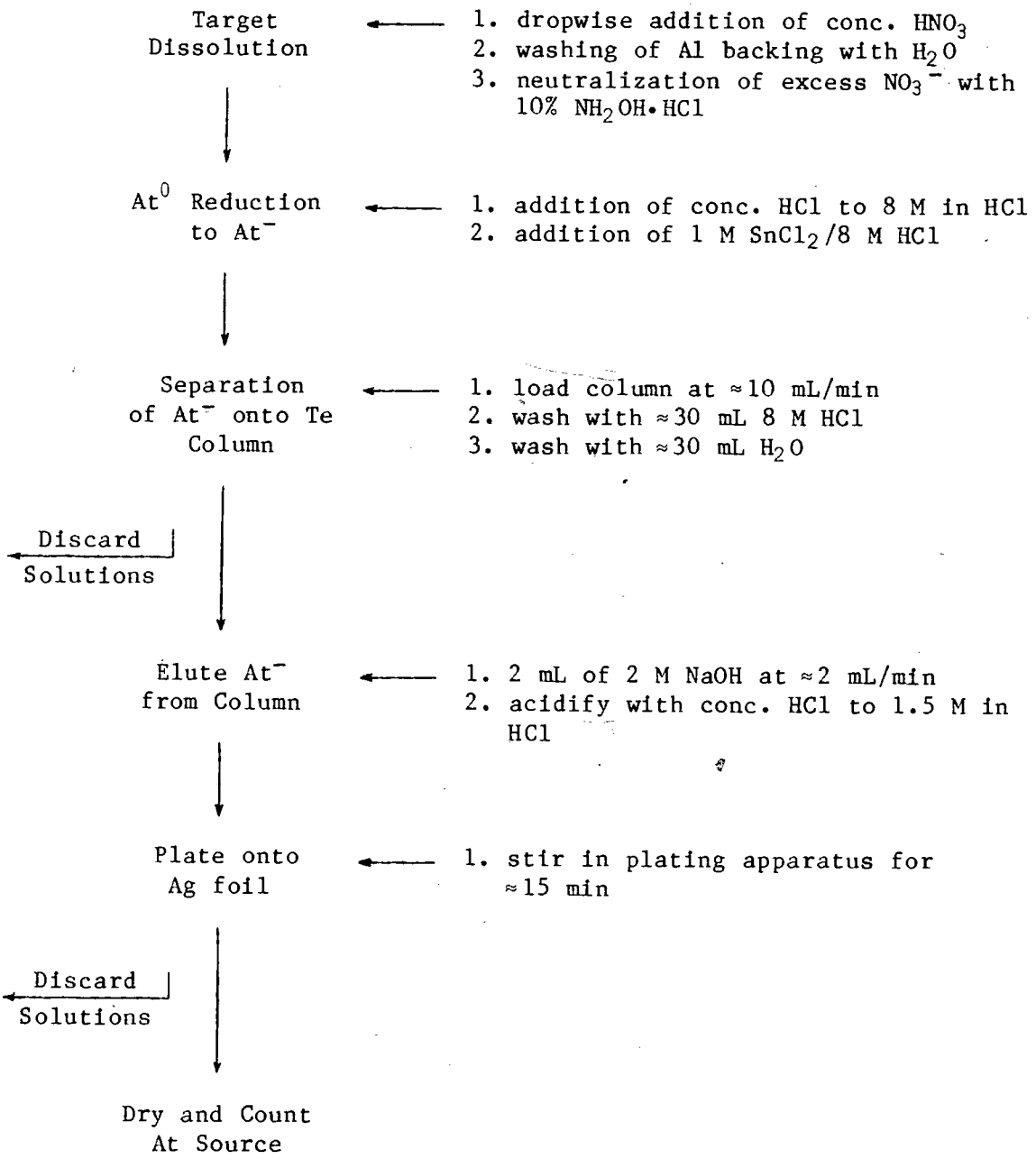

Figure 2 Schematic Representation of Chemical Separation

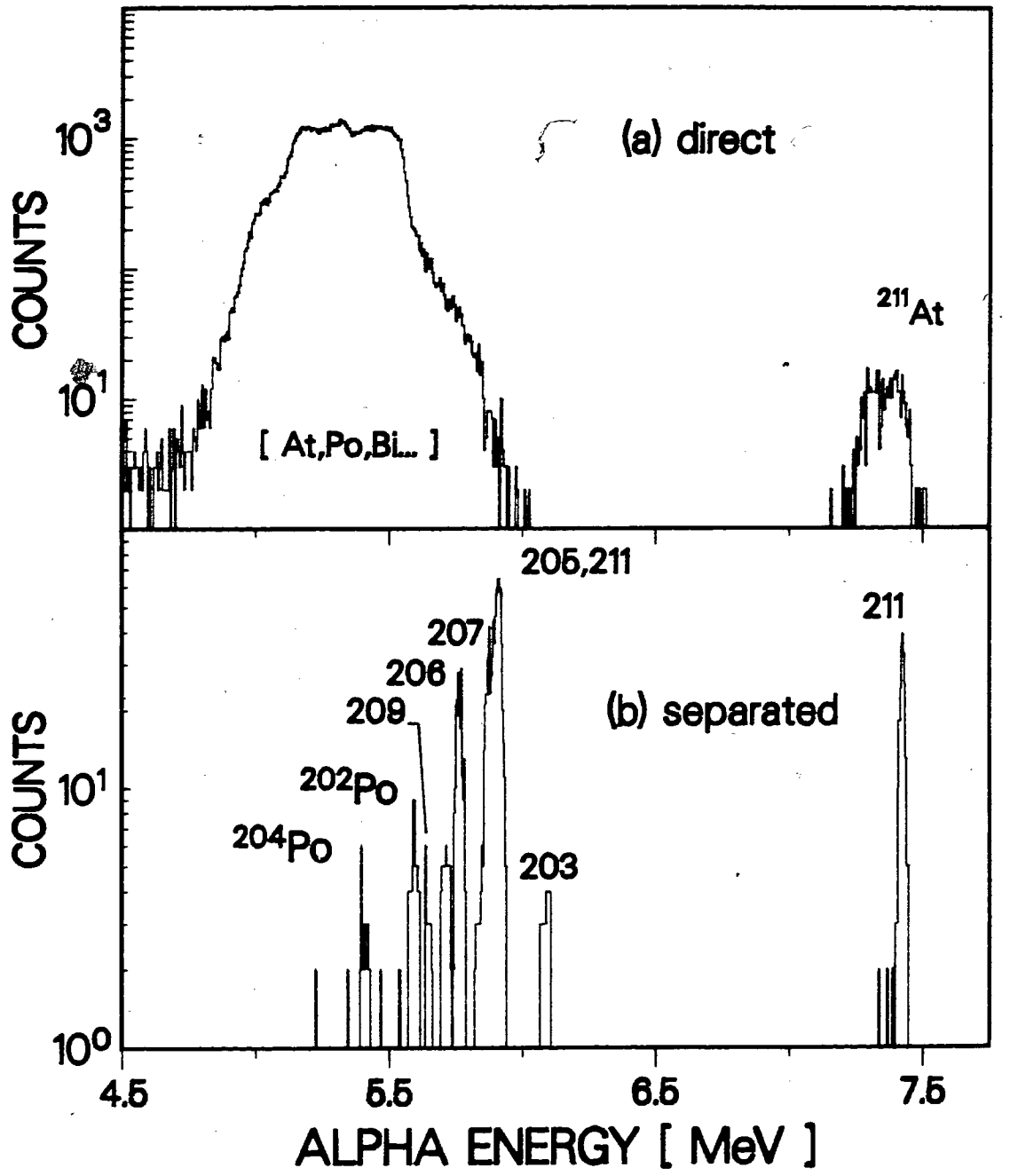

Figure 3 Directly Counted and Chemically-separated Astatine Alpha Spectra for 399 MeV Proton Runs

a: the 7.45 MeV is well separated from the other alpha activities

b: numbers above peaks refer to astatine nuclide identifications

Spectrum acquisition for the chemically-separated sources was more complex as both alpha and gamma spectra were acquired simultaneously. Alpha and gamma detection systems were calibrated separately since daughter gammas in coincidence with At alpha emitters have intensities too low to permit absolute count rate determination by coincidence methods. A special small vacuum chamber was constructed to hold the source in fixed close geometry with respect to a silicon surface barrier detector mounted in the chamber. The vacuum chamber was equipped with a thin (1/16") aluminum floor that allowed for the positioning of an external Ge(Li) gamma detector. The vacuum chamber is shown in Figure 4. The surface barrier detector was energy calibrated using a standard ^{241}Am source. Detection efficiency calibration was obtained by counting a ^{208}Po source of known activity and having the same physical dimensions as the plated astatine sources. The Ge(Li) detector was energy calibrated using seventeen γ-rays from a ^{226}Ra source. A least squares fit of ℓn(intensity) vs. $\ell n(\gamma$-energy) gave a relationship between relative detection efficiency and γ-ray energy for the detector. Standard ^{22}Na, ^{54}Mn, ^{60}Co, ^{133}Ba and ^{137}Cs sources were then counted in the same position as the astatine sources to obtain an absolute detection efficiency vs. γ-energy relation.

Alpha and gamma spectra were acquired for equal time intervals in separate memories of a multichannel analyzer. All spectra consisted of 1000 channels. Spectra were stored on floppy disk and transferred to an IBM 4341 for later analysis. The alpha spectra were sufficiently simple to allow analysis by hand. Alpha peaks were identified by their energies and half-lives and the channels summed to obtain count rates. Uncertainties were taken to be the square roots of the total counts in each peak. The

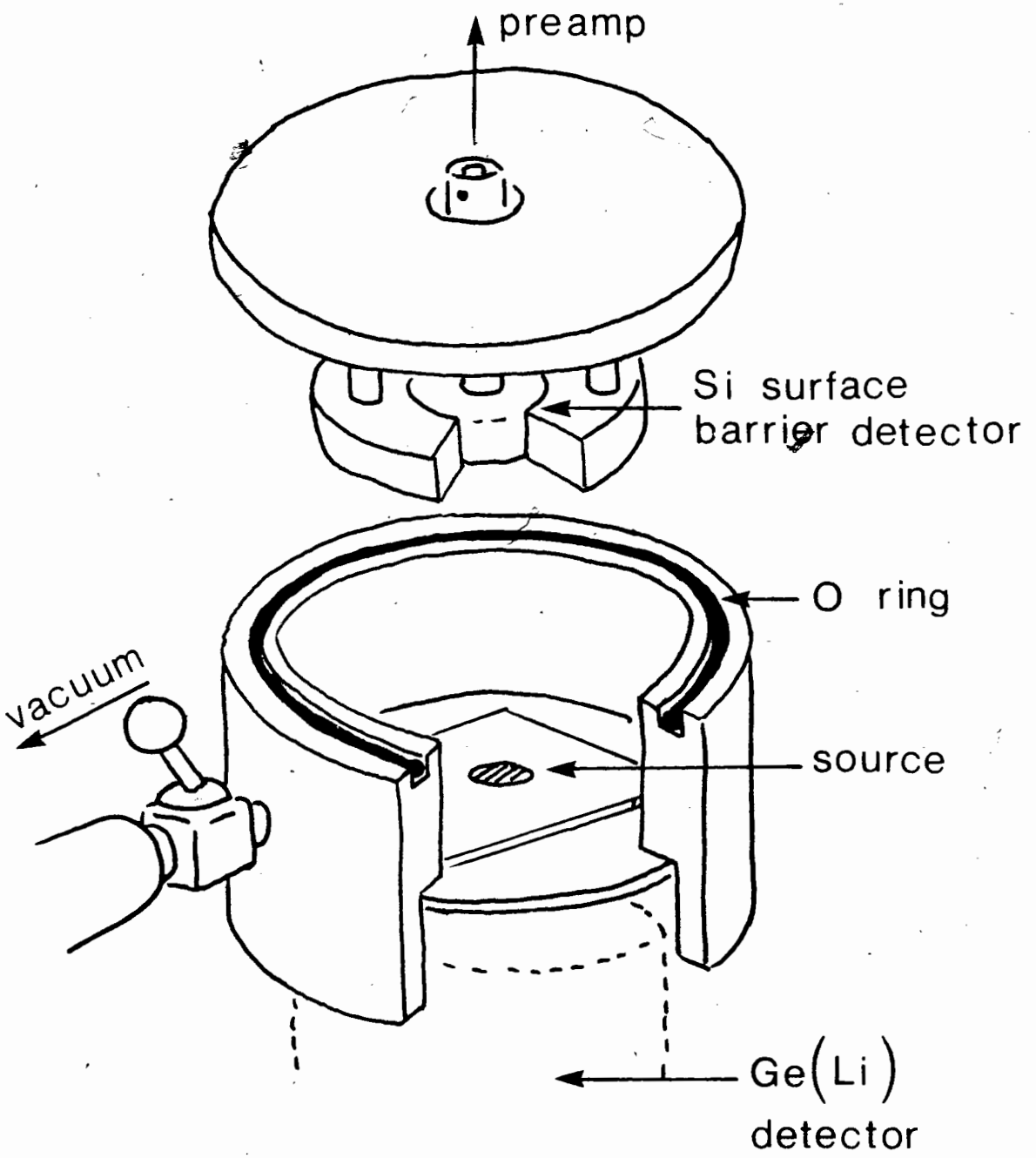

Figure 4 Vacuum Chamber Used in Simultaneous $\alpha-\gamma$ Counting

gamma spectra were analysed using the GAMANAL computer program[35] on an IBM 4341. Background subtraction, peak energy, peak integration and errors were determined by the program.

Cross section ratios for astatine nuclides with respect to the production cross section of ^{211}At were obtained by use of the following formulae:

$$\frac{\sigma_x}{\sigma_{211}{}_{At}} = \frac{\dfrac{A_{EOB}(x)}{(BR)_x \cdot (D_{eff})_x \cdot N \cdot \Phi_p \cdot (1-e^{-\lambda x t_B})}}{\dfrac{A_{EOB}(211)}{(BR)_{211} \cdot (D_{eff})_{211} \cdot N \cdot \Phi_p \cdot (1-e^{-\lambda_{211} t_B})}} \qquad (3)$$

where all factors are as defined for Equation 2 and the subscripts x and 211 refer to specific astatine nuclides. If branching ratio and detection efficiency corrections are made to the astatine activities, Equation 3 reduces to:

$$\frac{\sigma_x}{\sigma_{211}} = \frac{(\text{Absolute activity})_x \cdot (1-e^{-\lambda_{211} t_B})}{(\text{Absolute activity})_{211} \cdot (1-e^{-\lambda x t_B})} \qquad (4)$$

Reaction cross section ratios were calculated for x = 210-203 nuclides from both alpha and gamma spectra. Usually, a series of counts (3-7) was obtained for each proton energy; however, the 350 MeV run produced a low activity source and only one spectrum was obtained. The nuclides ^{211}At, ^{204}At and ^{203}At were identified only by their alpha activities, ^{210}At and ^{208}At were identified by gamma spectroscopy and the other nuclides identified by both methods. In addition, ^{210}At was measured indirectly by counting the activity of its daughter, ^{210}Po, after the ^{210}At had

completely decayed. The characteristics of the alpha and gamma activities used to identify the various At nuclides are given in Table VI, along with calculated reaction Q values.

Since the targets used for direct counting of ^{211}At and those used for cross section ratio determinations were of equivalent thickness, the absolute production cross section for any astatine nuclide at a specific proton energy is obtained by taking the product of the ratio and the ^{211}At cross section:

$$\sigma_x = \frac{\sigma_x}{\sigma_{211}} \times \sigma_{211} \qquad (5)$$

Typically, the ratio error was about ±20%, while the σ_{211} error was about ±10%, although, in some isolated cases, the uncertainties were larger. The ratio error resulted mainly from counting statistics, uncertainties in the literature branching ratios and the relative calibration of the two counting systems. The error in the ^{211}At cross section included uncertainties in detection efficiency (≈5%), beam integration (≈7%) and target thickness (≈6%). Individual uncertainties in counting statistics varied widely, from as low as ±1% for some high-intensity gammas to values of ±40% for some low-intensity alphas and gammas. The loss of At activity by recoil out of the target was estimated by counting a target backing foil for ^{211}At. The estimated loss of $\leq$1.5% was in good agreement with the $\leq$1% value determined for the ^{209}Bi(p,π^0)^{210}Po reaction[19]. No corrections for recoil have been made in the calculations.

Attempts to Detect Light Astatine Nuclides

Astatine nuclides lighter than ^{203}At could not be identified in either

Table VI

Decay Characteristics of Astatine Nuclides[a]

Nuclide	$t_{1/2}$	E_α (MeV)	B.R. (%)	E_γ (keV)	B.R. (%)	$Q(p,\pi^- xn)$[d] (MeV)
^{211}At	7.21 h	5.866 7.450[b]	41.90 57.20			
^{210}At	8.30 h			245.3 1181.4	79.40 99.30	-138.6
^{210}Po	138.00 d	5.304	99.90			
^{209}At	5.42 h	5.647	8.40[c]	545.0 781.9 790.2	94.40 86.60 66.00	-145.7
^{208}At	1.63 h			177.0 660.0 685.0	46.00 90.10 97.90	-154.1
^{207}At	1.81 h	5.759	11.50[c]	588.4 814.5	22.00 49.00	-161.5
^{206}At	31.40 m	5.703	0.96	395.5 477.1 700.7	47.80 85.90 97.00	-170.1
^{205}At	26.20 m	5.901	10.00	520.5 628.8 669.4 719.3	3.67 4.76 8.40 28.00	-178.0
^{204}At	9.30 m	5.948	4.40			-187.0
^{203}At	7.30 m	6.086	31.00			-197.1
^{202}At	3.00 m	6.227	15.00			-204.6
^{201}At	1.50 m	6.342	71.00			-212.7

[a] All values from Ref. 25 unless otherwise indicated.

[b] From decay of ^{211}Po daughter; $t_{1/2}$ = 0.525 sec.

[c] From Ref. 20 and 33.

[d] Calculated using mass values of Ref. 36.

the gamma or alpha spectra of the chemically-separated samples due to their short half-lives. Attempts were therefore made to detect the short-lived astatines by a direct counting method. A very thin ($\approx$100 $\mu g/cm^2$) bismuth target, evaporated onto a 200 $\mu g/cm^2$ carbon backing, was mounted on a movable arm in the SFU scattering chamber at TRIUMF. This movable target could be positioned in the proton beam or in front of a Si surface barrier detector at 30° from the beam. A computer-controlled cycling sequence was used to, in turn, irradiate the target (60 sec), move the target to the detector (30 sec) and count the target (60 sec). This sequence was cycled and multiple spectra could be collected without turning the beam off. Alpha spectra were collected for proton energies of 210, 300, 399, 450 and 481 MeV, either singly or by summing spectra from six cycles[34]. Though polonium nuclides with half-lives as short as 5.5 sec were detected (from the series of (p,xn) reactions), no astatine activity was found. Nonetheless, by using the lower limits of detection for the short-lived poloniums ($\approx$10 counts/sec), upper limits could be placed on the light At cross sections. These were estimated to be $\lesssim\approx$50 μb for ^{202}At, $\lesssim\approx$7 μb for ^{201}At and $\lesssim\approx$15 μb for ^{200}At. The cross sections obtained for polonium nuclides in the series of (p,xn) reactions, with x = 0-14, have been published elsewhere[34].

SECONDARY REACTION CALCULATIONS

Introduction

The astatine activity measured in the present work results from three major reaction processes. In addition to the primary reactions $^{209}Bi(p,\pi^-xn)^{210-x}At$, astatine can also be produced by two secondary (two-step) reaction mechanisms: $^{209}Bi(p,\alpha X)$, followed by $^{209}Bi(\alpha,xn)^{213-x}At$, and $^{209}Bi(p,^3HeX)$, followed by $^{209}Bi(^3He,xn)^{212-x}At$. Similar reactions involving lithium or heavier fragments are expected to be insignificant since $^{209}Bi(p,LiX)$ production is of the order of $\lesssim 1\%$ of the alpha production at the proton energies under consideration[37,38].

Production of astatine by protons on bismuth has previously been measured at Dubna[39-41] and Orsay[42-44] in the energy range 60-660 MeV. Astatine production in these thick target measurements was attributed to the secondary reactions involving intermediate alphas. However, Kurchatov et al.[40] noted that the light ($A \leq 205$) astatine nuclei could not be produced in quantity by secondary processes and attributed their formation to the primary (p,π^-xn) reactions. The purpose of the Dubna and Orsay measurements was to deduce the energy distribution of the emitted alpha particles from the oberved At nuclide production ratios and previously measured (α,xn) excitation functions. Reversing this type of calculation allows estimation of secondary At yields if the (p,α) energy-dependent cross section and the (α,xn) excitation functions are known.

The Secondary Cross Section

Metzger and Miller[45] have expressed the cross section for production

of secondary nuclei in thick targets as

$$\sigma_{sec} = \int_0^\infty \sigma_f(E_f) P_c(E_f) dE_f \qquad (6)$$

where $\sigma_f(E_f)$ is the angle-integrated, energy-dependent cross section for fragment production as a function of fragment energy (in units of cross section per energy). $P_c(E_f)$ is the probability that a fragment of initial energy (E_f) will interact with a second target nucleus at some point in its range to form a secondary compound nucleus. This probability is in turn expressed as

$$P_c(E_f) = N \int_0^{E_f} \sigma_c(E_f) dr_f \qquad (7)$$

where N is the number of target nuclei per cubic centimeter, $\sigma_c(E_f)$ is the cross section for formation of the secondary compound nucleus (in units of cm^2) and dr_f is an element of the fragment range in centimeters. Since the integral in Equation 7 is in terms of fragment energy, dr_f is eliminated by using an appropriate range-energy relation ($-dE_f/dr_f$). The preceding equations show that, in order to successfully calculate a production rate by secondary reactions, three things must be known: first, the production rate and energy distribution of the secondary fragments; second, the energy dependence of that fragment's interaction with target nuclei; and, third, a relationship describing the energy loss of the fragment as it travels through the target. For the present purpose of calculating secondary astatine production, the first and second relations were obtained from available experimental data, while the energy loss relation used was a standard, classical formula.

The (p,α) and (p,^{3}He) Energy Distributions

While there are no experimental determinations of the inclusive (p,α) and (p,^{3}He) fragment spectra from bismuth in the proton energy region of this study, both fragment energy distributions have been measured at 90 MeV[46]. Also, Segel et al.[47] have measured charged particle spectra from protons on ^{208}Pb at 164 MeV. The alpha and ^{3}He energy distributions from bismuth are expected to be similar.

The general shapes of inclusive fragment spectra ($d\sigma/dE$ vs. E) have been shown to remain essentially the same over bombardment energies of several hundred MeV, while the absolute magnitude of the fragment production cross section increases with beam energy[37]. Figure 5 shows typical angle-integrated shapes for both fragment distributions, as obtained from the data of Segel et al.[48]. For the purpose of secondary yield calculations, the shapes of the fragment spectra above 20 MeV were approximated by the form

$$\frac{d\sigma}{dE_f}\left(\frac{mb}{MeV}\right) = A \exp\{-B(E_f - 20\ MeV)\} \qquad (8)$$

A lower energy cutoff of 20 MeV was chosen to eliminate the need for fitting the evaporative "peak" of the distributions. Since this energy roughly corresponds to the threshold of the ^{209}Bi(α,2n)^{211}At reaction, α energies below 20 MeV make no contribution to any secondary nuclides observed.

The parameter B in Equation 8 was estimated to be 0.077 MeV^{-1} for alpha particles and 0.028 MeV^{-1} for ^{3}He particles from the 90 MeV and 164 MeV spectra.

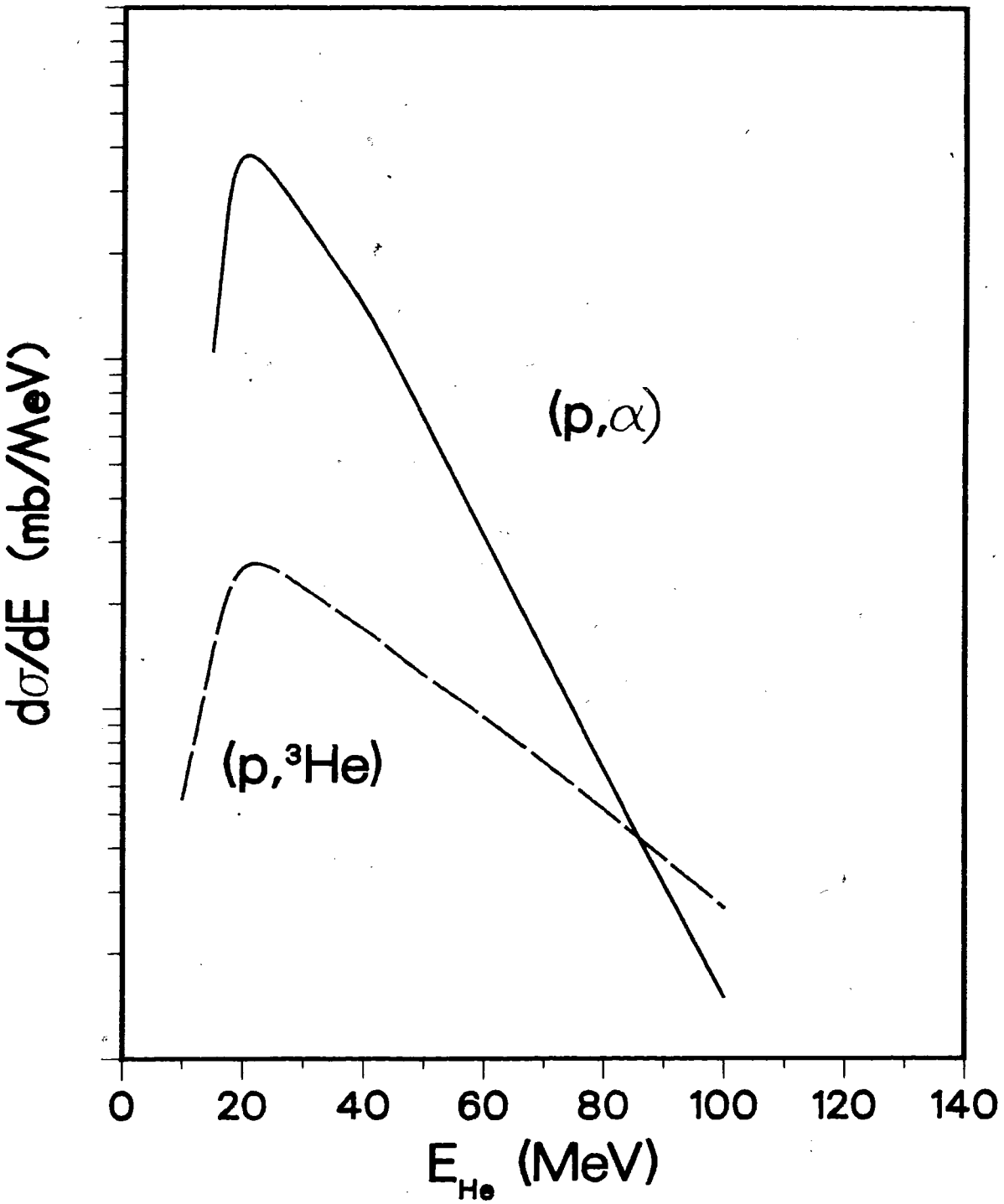

Figure 5 Shapes of the Helium Fragment Energy Distributions Used in Secondary Calculations (from Ref. 47)

The parameter A was not fixed at any particular value but was normalized to experimentally observe ^{211}At yields for each calculation at specific beam energies and target thicknesses. The particulars of the normalization will be discussed later. For ^{3}He distributions, A was fixed at 0.7% of the normalized value used for alpha particles, in keeping with lower (p,^{3}He) cross sections[37,46,47].

The (α,xn) and (^{3}He,xn) Excitation Functions

The experimental excitation functions of ^{209}Bi(α,xn)$^{213-x}$At for x = 2-7[49-52] were fit to semiempirical functions based on the Jackson model of successive neutron evaporation[49,53]. The collected experimental data is listed in Table VII.

The Jackson model was first proposed to schematically describe (p,xn) and (p,pxn) excitation functions by the successive evaporation of neutrons from an excited compound nucleus formed after a prompt knock-out event. It has since been used to describe other reactions involving neutron emission, including the (α,xn) reactions[42,43,53]. According to the model, the cross section for a particular (α,xn) reaction is given by

$$\sigma(\alpha,xn) = \sigma_c(E_o) \sum_{i=0}^{x} q(i)\langle P(E,x-i)\rangle \qquad (9)$$

where $\sigma_c(E_o)$ is the reaction cross section for an incident α of energy E_o, q(i) is the relative probability of the emission of i prompt neutrons and $\langle P(E,x-i)\rangle$ is the averaged neutron evaporation probability. The probability of emitting at least i neutrons is given by

$$P_i = 1 - \exp\{-\Delta_i\} \sum_{i=0}^{2i-3} \frac{(\Delta_i)^n}{n!} \qquad (10)$$

Table VII

Collected Experimental Cross Sections for

(α,xn) and (^{3}He,xn) Reactions on ^{209}Bi [49-52]

E_p (MeV)	σ (mb)	E_p (MeV)	σ (mb)	E_p (MeV)	σ (mb)
		(α,2n)			
20.2	1	28.7	780	34.8	390
20.6	1.4	29.3	837	35.5	370
21.2	10	29.6	900	35.6	315
21.6	20	29.7	850	35.7	344
21.8	42	29.8	870	36.4	265
22.4	100	29.9	900	36.7	250
22.6	113	30.4	905	37.2	215
23.0	110	30.5	890	37.3	226
23.1	160	30.7	890	38.0	170
23.5	250	31.0	909	38.4	145
24.0	205	31.4	860	38.8	150
24.2	291	31.7	850	40.0	104
24.6	290	32.2	810	40.1	134
24.7	375	32.3	750	41.0	110
25.4	406	32.6	750	43.3	92
25.5	450	33.0	713	49.0	52
25.7	521	33.1	620	58.0	28
26.1	573	33.3	630	65.0	18
26.5	580	33.6	610	71.0	10
26.7	670	34.0	480	78.0	8.5
27.4	706	34.2	499	82.5	5
27.6	690	34.5	460	89.5	4.5
27.7	750	34.6	470	95.0	3.8
28.6	816	34.6	390	99.5	3.4
		(α,3n)			
28.6	4	33.3	530	40.0	1100
28.7	3	33.6	610	40.1	1168
29.6	13	33.9	618	41.0	1172
29.7	7	34.0	730	43.3	977
29.8	11	34.2	715	44.2	986
29.9	15	34.6	820	49.0	320
30.4	36	34.8	930	49.7	305
30.5	60	35.5	1100	54.6	150
30.7	50	35.6	985	58.0	200
31.0	91	35.7	985	60.1	77
31.4	170	36.4	1150	65.0	110
31.7	160	36.7	1110	71.0	105

Table VII (Cont'd)

32.2	280	37.2	1205	78.0	100
32.3	350	37.3	1116	82.5	73
32.6	370	38.0	1240	89.5	52
33.0	396	38.6	1179	95.0	60
33.1	530	38.8	1270	99.5	52
		(α,4n)			
40.0	57	49.7	1036	65.5	323
41.0	151	54.6	1034	69.6	150
43.3	391	58.0	550	71.0	220
44.2	344	60.1	640	74.0	110
49.0	1000	65.0	300	79.4	72
		(α,5n)			
49.0	14	69.6	508	82.5	240
54.6	277	71.0	400	89.5	225
60.1	709	74.0	405	95.0	230
65.0	650	78.0	350	99.5	195
65.5	736	79.4	296		
		(α,6n)			
58.0	5.4	71.0	440	82.5	180
65.0	220	74.0	603	89.5	110
65.5	229	78.0	350	95.0	100
69.6	569	79.4	484	99.5	85
		(α,7n)			
65.0	9	82.5	560	99.5	300
71.0	42	89.5	500		
78.0	300	95.0	390		
		(^{3}He,3n)			
24.7	236	39.7	185	60.6	72
29.8	1200	44.6	87	65.3	77
34.4	516	56.0	70		
		(^{3}He,4n)			
29.8	186	49.5	477	65.3	240
34.4	906	56.0	326		
39.7	802	60.6	292		
		(^{3}He,5n)			
34.4	22	49.5	966	65.3	350
39.7	361	56.0	644		
44.6	1164	60.6	431		

Table VII (Cont'd)

		(^{3}He,6n)			
56.0	681	60.6	1105	65.3	942

where

$$\Delta_i = \frac{E^* - \sum_{i}^{i} S_i}{\tau} \qquad (11)$$

$E^* \equiv$ excitation energy;

$S_i \equiv$ binding energy of ith neutron;

$\tau \equiv$ nuclear temperature $(E^*/a_\rho)^{1/2}$, where $a_\rho \equiv$ level density parameter.

The probability of evaporating exactly i neutrons is defined as the difference between P_i and $P_{(i+1)}$. For the current calculations, the reactions were assumed to occur entirely by evaporative processes, eliminating the q(i) term from Equation 9. The formula for the reaction cross section, $\sigma_c(E_o)$, was taken from Shapiro[54]:

$$\sigma_c(E_\alpha) = \pi(R+\lambda)^2\left(1-\frac{B}{E_\alpha}\right) \qquad (12)$$

where $R \equiv$ target nuclear radius;

$\lambda \equiv$ rationalized projectile wavelength;

$B \equiv$ Coulomb barrier.

Since the purpose of fitting the experimental data were merely to provide a descriptive function, rather than to extract meaningful parameters, four arbitrary proportionality coefficients were introduced into the final form of the fit expression,

$$\sigma(\alpha,xn) = \sigma_c\{a\cdot(E_\alpha)^b\cdot P_{(x)} - c\cdot(E_\alpha)^d\cdot P_{(x+1)}\} \qquad (13)$$

where σ_c is described by Equation 12 and $P_{(x+1)}$ and $P_{(x)}$ are

described by Equations 10 and 11. The coefficients a, b, c and d, as well as the level density parameter (a_ρ) and the target radius (R) were fit by a non-linear iterative least squares method with the ITER computer program provided by Dr. K.E. Newman of Simon Fraser University. The six parameters were not all obtained from simultaneous fits. Generally, values of the parameters R and a_ρ were first determined so as to reasonably approximate the "peak" region of the excitation functions. These values were then fixed and the parameters a, b, c and d were varied to approximate the high energy tails of the excitation functions. The use of these four coefficients was necessary to account for contributions from "direct" emission of neutrons described by the term q(i) in Equation 4. In the cases where few experimental data points were available, not all of the excitation functions could be fit with all six parameters. All values of atomic masses and neutron binding energies used were taken from the 1977 compilation of Wapstra and Bos[36]. The final best fits are shown with the experimental data in Figure 6. The values of the fit parameters are given in Table VIII. The parameter R has been converted to the more familiar R_o by the relation $R = R_o A^{1/3}$. While no effort was made to limit any of the parameters to "meaningful" values, the final magnitudes of R_o and a_ρ are not unreasonable in comparison to accepted values.

The Charged Particle Stopping Power

In order to account for alpha and ^{3}He particle energy losses in the target and permit integration of Equation 7 by substituting particle energy for particle range, the non-relativistic, charged particle, stopping power formula of Bethe[55] was used:

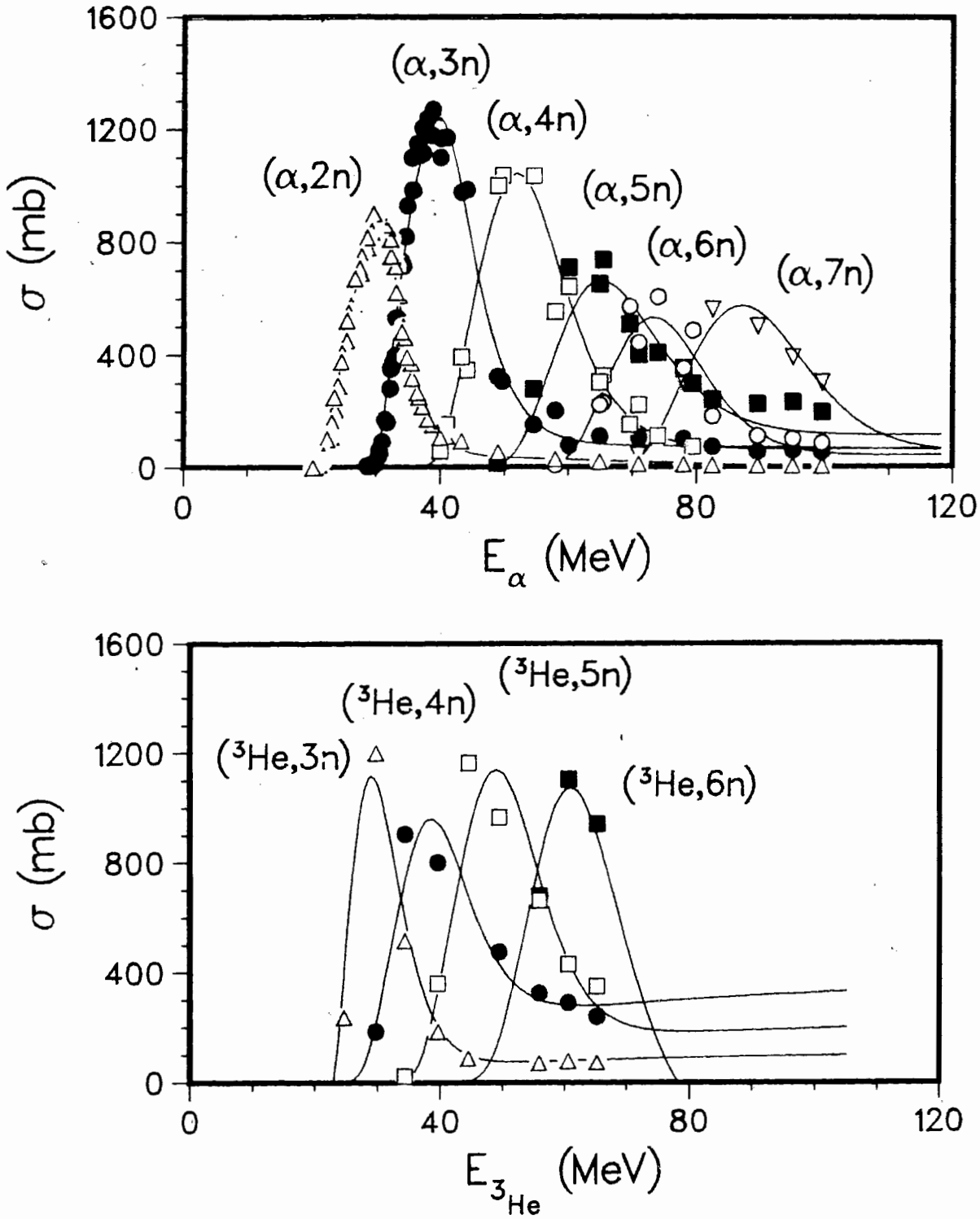

Figure 6 The (α,xn) and (^{3}He,xn) Excitation Functions on ^{209}Bi. Solid lines represent least squares fits.

Table VIII

Calculated Parameters of Least Squares Fits of the

(α,xn) and $(^3He,xn)$ Excitation Functions

	R_o ($\times 10^{-13}$ cm)	a_p (MeV^{-1})	a	b	c	d
$(\alpha,2n)$	1.64	14.20	1.00	1.38×10^{-3}	0.88	2.85×10^{-2}
$(\alpha,3n)$	1.64	14.20	0.07	0.56	0.06	0.58
$(\alpha,4n)$	1.64	14.20	0.67	-	0.64	-
$(\alpha,5n)$	1.64	14.20	0.45	8.56×10^{-4}	0.39	8.98×10^{-3}
$(\alpha,6n)$	1.04	26.05	0.98	-	0.94	-
$(\alpha,7n)$	1.19	25.01	0.98	-	1.00	-
$(^3He,3n)$	1.64	18.80	2.31	-	2.37	-
$(^3He,4n)$	1.64	18.80	0.92	-	0.79	-
$(^3He,5n)$	1.57	23.99	0.95	-8.40×10^{-4}	0.86	-9.80×10^{-4}
$(^3He,6n)$	1.57	23.99	0.89	-	1.00	-

$$\frac{-dE}{dr} = \frac{4\pi e^4 z^2 ZN}{m_e v^2} \ln\left\{\frac{2m_e v^2}{\langle I\rangle}\right\} \qquad (14)$$

where E ≡ charged particle energy;

r ≡ distance travelled by charged particle;

e ≡ elementary charge;

z ≡ particle unit charge;

Z ≡ target unit charge;

N ≡ atomic density of target (atoms/cm^3);

m_e ≡ electron mass;

v ≡ particle velocity;

$\langle I\rangle$ ≡ mean ionization potential of target.

A value of $\langle I\rangle$ = 0.763 keV for bismuth was taken from the calculation of J.F. Ziegler[56].

After appropriate substitutions are made for the terms in Equation 14, the stopping power functions for alphas and ^{3}He particles in bismuth are reduced to the form:

$$\left(\frac{-dE}{dr}\right)_\alpha = \frac{0.907 \ln(0.719\ E_\alpha)}{E_\alpha} \frac{MeV}{mg/cm^2} \qquad (15)$$

$$\left(\frac{-dE}{dr}\right)_{^3He} = \frac{0.620 \ln(0.954\ E_{^3He})}{E_{^3He}} \frac{MeV}{mg/cm^2} \qquad (16)$$

Calculation of Secondary Yields

Calculations of the secondary production cross sections of astatine nuclides were performed by numerical integration of Equations 6 and 7. The

(p,α) energy spectrum described by Equation 8, from 20 to 120 MeV, was first divided into n intervals $(dE_\alpha)_i$ of about 4 MeV width. The average alpha production cross section $(\bar{\sigma}_{(p,\alpha)})_i$ and the corresponding energy $(\bar{E}_\alpha)_i$ were calculated for each interval. The alphas were then followed on their path through the target which was in turn divided into m slices, $(dr)_j$ thick. The energy of the alpha particles in the middle of each thickness slice was calculated from their initial energy $(\bar{E}_\alpha)_i$ and the energy loss given by the stopping power formula (Equation 15). The probability of an alpha interacting in a particular thickness slice was taken as the product of the number of target nuclei in the slice (n_j) and the cross section for a particular (α,xn) reaction at the alpha energy in that slice, $\sigma_j(E_j)_{(\alpha,xn)}$. The total probability of an alpha with an initial average energy, $(\bar{E}_\alpha)_i$, interacting with the target by means of a specific (α,xn) reaction was described by:

$$P_i = 1-\exp\{-\sum_j n_j\sigma(E_j)_{(\alpha,xn)}\} \qquad (17)$$

The calculation proceeded in a stepwise integration through the alpha fragment spectrum summing the cross section from each energy interval to give a final, total production cross section for a specific nuclide:

$$\sigma_{TOT}(p,\alpha)(\alpha,xn) = \sum_i P_i(\bar{\sigma}_{(p,\alpha)})_i \qquad (18)$$

The calculation was performed on an IBM 4341 computer. The input parameters were:

n ≡ the number of energy slices;

m ≡ the number of thickness slices;

A ≡ the parameter describing the magnitude of the (p,α) spectrum;

t ≡ the target thickness.

The parameters n and m were varied to observe the sensitivity of the calculation to the number of intervals used. Dividing both the energy spectrum and the target thickness into 1000 intervals greatly increased the running time of the program but produced no change in the result (to two significant figures) from that obtained by using 25 intervals. The values of n and m were set to 25 for all calculations. Figure 7 displays the steps of the calculation schematically.

Thin Target Calculations

The preceding calculation is strictly valid only for thick targets, where the alpha fragment range and flux reach saturation at all emission angles and an angle integrated form of $\sigma_f(E_f)$ can be used in Equation 1. For thin target cases, σ_f must be replaced by a function having both energy and angular dependence, $\sigma_f(E_f,\theta_f)$, in order to account for target thickness variation with emission angle. While a rigorous treatment requires the added complexity of angular dependence, several factors allow the thick target calculations to be used as a good first order approximation of secondary yields in the present case.

First, the energy distribution of low energy fragments does not change significantly with emission angle. The distribution of low energy fragments is essentially isotropic. The shorter range of these fragments makes the production of heavier secondary At nuclides least susceptible to thickness effects.

Second, the emission of higher energy fragments, responsible for lighter At nuclide production, is greatest at forward angles. Because of

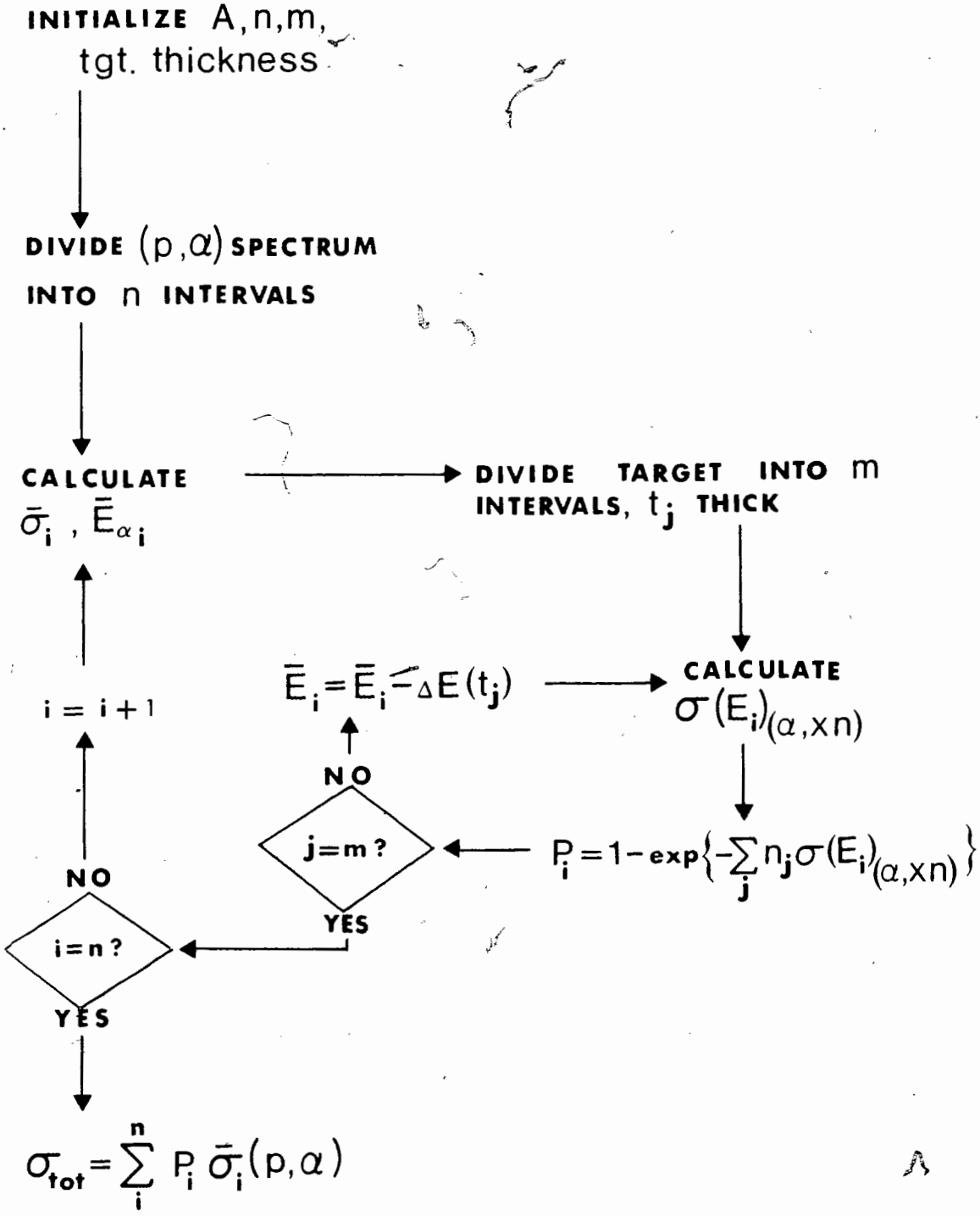

Figure 7 Schematic Representation of the Secondary Calculations

(see text for explanation)

the greater range of these fragments, small changes in emission angle will not significantly increase the production of secondaries in a thin target.

Finally, in this specific case, the detection of ^{211}At produced exclusively by secondary reactions allows all calculated secondary yields to be normalized to the observed ^{211}At yield, thus "averaging" the effects of thickness variation with angle.

The results of both thick and thin target secondary yield calculations are shown in Figure 8. The yields from ^{3}He fragments were calculated in a manner analogous to the alpha fragment calculations and summed with the alpha yields.

The normalization of each secondary yield calculation to the experimentally observed ^{211}At yields was accomplished by using an "effective" target thickness as a program input parameter. Literature values of ^{211}At production yields from 60 to 660 MeV protons[39-44] were used to obtain a linear relationship for ^{211}At production in thick targets as a function of proton energy (see Figure 9). Using the relation,

$$\sigma_{^{211}\mathrm{At}}\ (\mathrm{mb}) = m \cdot E_p\ (\mathrm{MeV}) + b$$

where $m = 0.0546 \pm 0.003$ and

$b = 0.757 \pm 0.385$,

thick target ^{211}At yields were calculated for the specific proton energies of the present work. Secondary calculations were then performed varying the input parameter A (the magnitude of the (p,α) cross section) until agreement was reached with the calculated ^{211}At yields. In this manner, values of A were obtained for each proton energy. These were subsequently

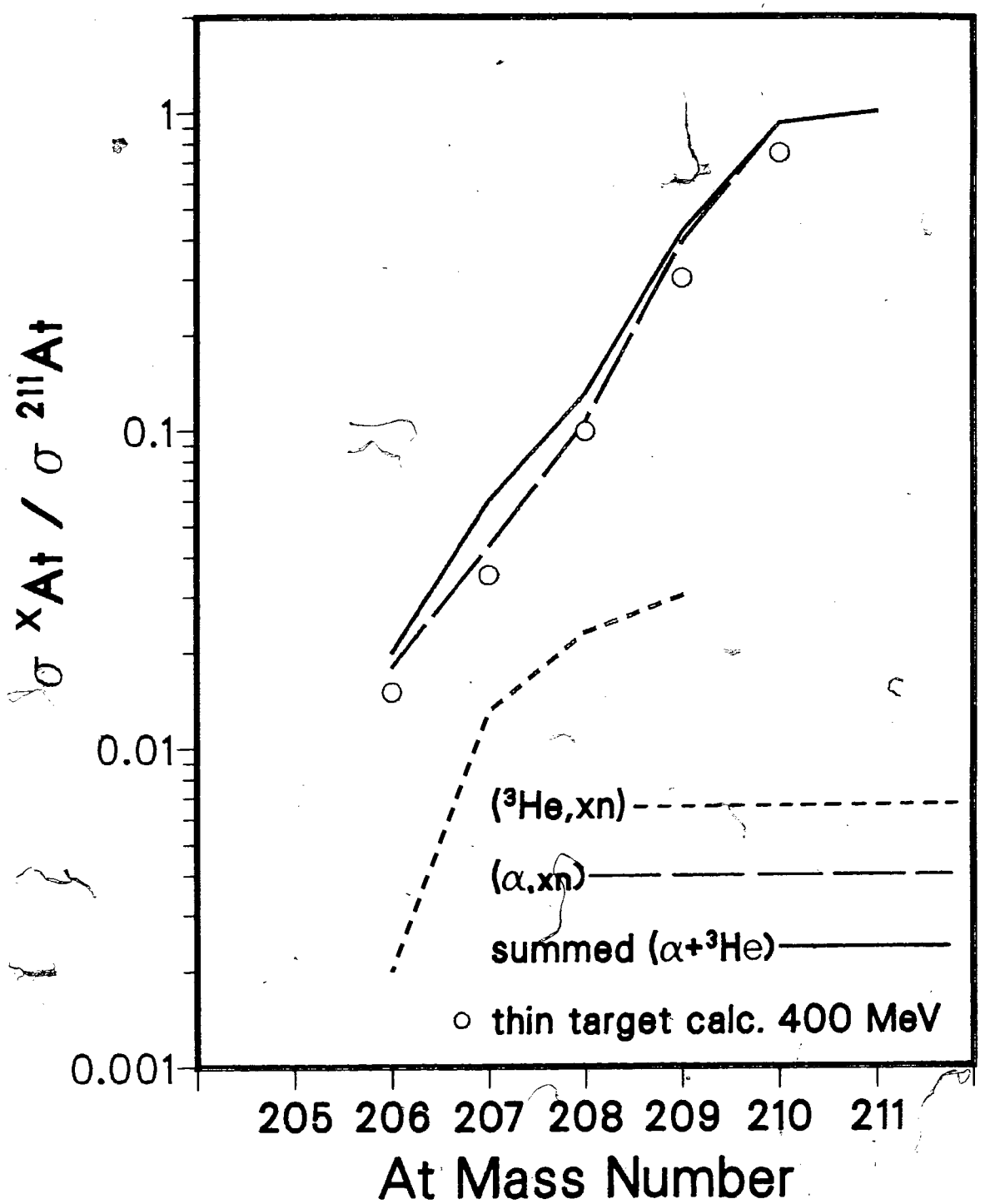

Figure 8 Relative Secondary Cross Section Ratios Calculated for Thick Targets and One Typical Thin Target. Contributions from ^{4}He and ^{3}He fragments are shown.

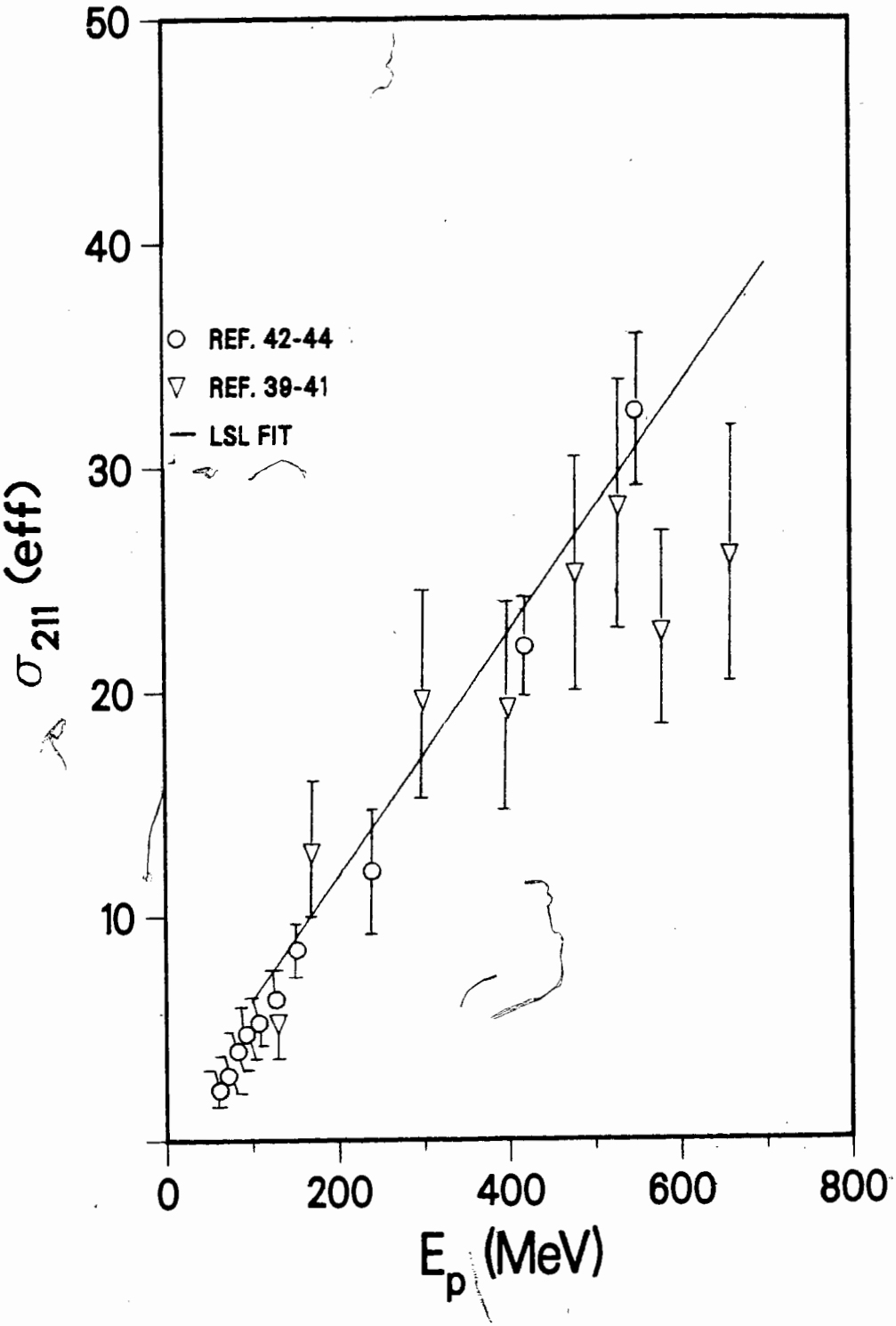

Figure 9 Thick Target ^{211}At Cross Sections (Ref. 35-40)

used in thin target calculations where the target thickness input parameter was varied until agreement was reached with the observed ^{211}At yield from the thin target. This "effective" target thickness and the calculated parameter A were then used in subsequent calculations of the yields of other At nuclides at that proton energy. Table IX gives the calculated values of ^{211}At yields and A parameters for various energies.

Comparison with Experimental Data

In order to assess the reliability of the secondary calculations, comparisons were made with experimental determinations of astatine yields from References 35-40. Due to the change in accepted values of At nuclide branching ratios since the earlier measurements, the literature data were corrected to reflect branching ratios used in this work. Table X lists the correction factors for relative cross sections (σ^{A}At/σ^{211}At). The correction factors were computed using the formula:

$$\text{Correction factor} = \frac{\dfrac{\text{B.R. } ^{211}\text{At (this work)}}{\text{B.R. } ^{211}\text{At (lit)}}}{\dfrac{\text{B.R. } ^{A}\text{At (this work)}}{\text{B.R. } ^{A}\text{At (lit.)}}}$$

The relative cross sections obtained from the literature are multiplied by the correction factors to obtain values based on the branching ratios used in this work.

Figure 10 shows corrected relative cross sections from Lefort et al.[43] along with the values predicted in this work as a function of astatine mass number. Except for 150 MeV, all proton energies are below the pion production threshold. The astatine products are from secondary reactions only.

Table IX

Summary of Calculated ^{211}At Cross Sections on Thick Targets

E_p (MeV)	σ^{211}At (Thick Target) (mb)	A (mb/MeV)
120	5.8	3.9
160	8.0	5.3
180	9.1	6.1
188	9.5	6.4
200	10.2	6.8
210	10.7	7.2
214	10.9	7.3
225	11.5	7.7
252	13.0	8.7
300	15.6	10.5
350	18.4	12.3
399	21.0	14.1
450	23.8	15.9
480	25.5	17.1

Table X

Correction Factors for Branching Ratios in Literature Values of Relative Astatine Yields

Relative Yield	Correction Factor	
	Ref. 43	Ref. 41
$\frac{\sigma^{210}At}{\sigma^{211}At}$	× 1.01	-
$\frac{\sigma^{209}At}{\sigma^{211}At}$	× 1.08	× 0.61
$\frac{\sigma^{208}At}{\sigma^{211}At}$	× 1.11	× 0.19
$\frac{\sigma^{207}At}{\sigma^{211}At}$	× 0.89	× 0.89
$\frac{\sigma^{206}At}{\sigma^{211}At}$	-	× 0.96
$\frac{\sigma^{205}At}{\sigma^{211}At}$	-	× 1.84
$\frac{\sigma^{204}At}{\sigma^{211}At}$	-	× 1.05
$\frac{\sigma^{203}At}{\sigma^{211}At}$	-	× 0.46

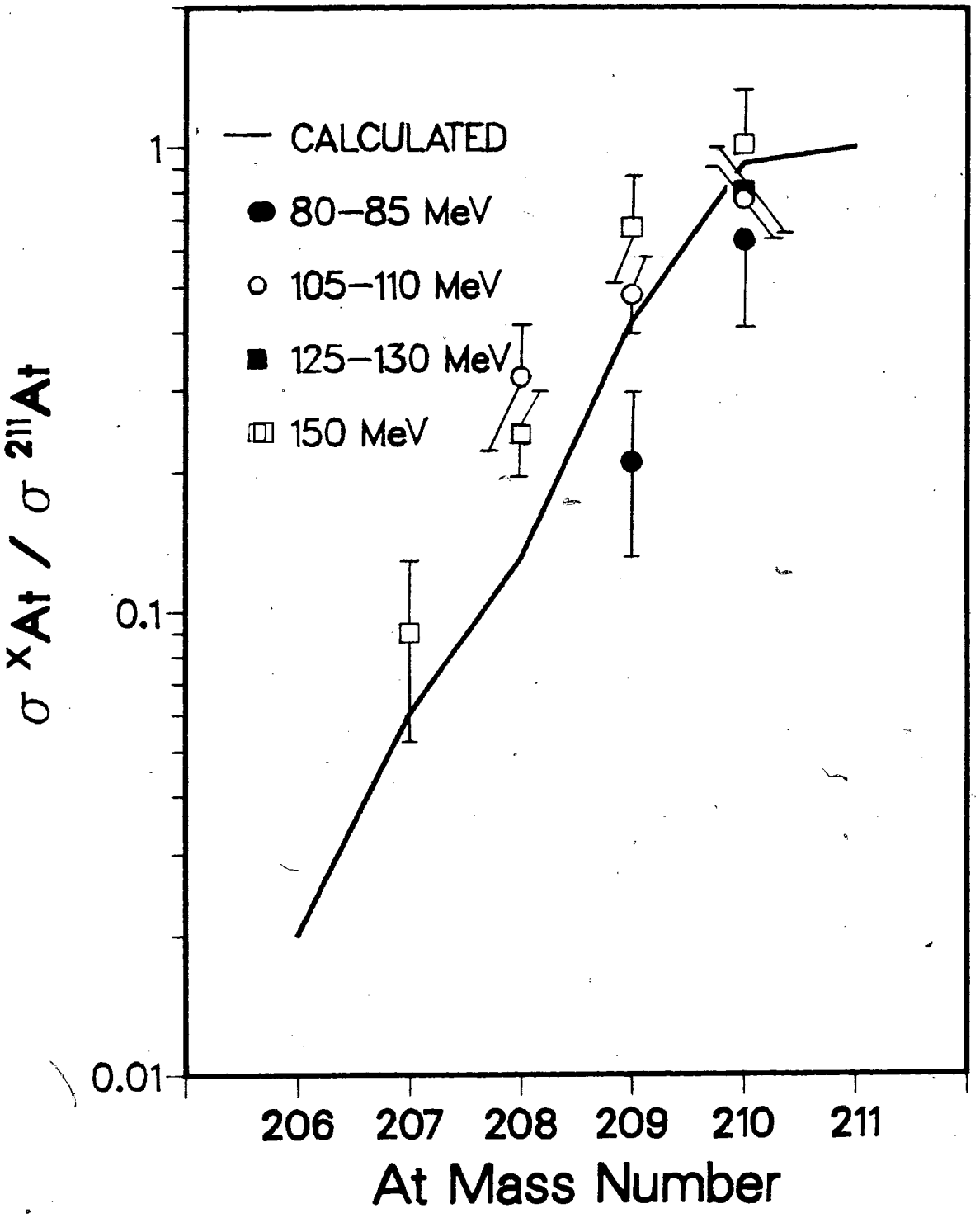

Figure 10 Calculated Secondary Ratios Compared to the Secondary Experimental Data of Ref. 43

At 150 MeV, only ^{210}At and ^{209}At can be produced by a (p,π^-xn) reactions. ^{208}At and ^{207}At are produced by secondaries. Generally, the agreement between calculated and experimental values is very good.

Higher energy proton data from the work of Li et al.[41] are displayed in Figure 11. Here, with the exception of the 120 MeV data, all proton energies are well above the pion production threshold and astatine can be produced by the (p,π^-xn) reactions. For nuclides with mass $\leq$207, the relative cross sections have been averaged over all proton energies. Figure 11 shows what appears to be two different mass distributions. For nuclides heavier than ^{207}At, the secondary calculations are in excellent agreement with experiment. However, beginning with ^{207}At, the lighter nuclides display a trend to increased cross section with decreasing mass number. this can be explained by a large cross section for the (p,π^-xn), $x \geq 3$, reactions even at high proton energies, that completely overwhelms the secondary reaction channels.

A further comparison with experiment is shown in Figure 12. Here, only ^{209}At and ^{207}At relative cross sections at a proton energy of 120 MeV were obtained ~~at~~ IUCF. While the general trend is represented by the calculated curves, the agreement is not very good for the ^{207}At cases. Due to low activities and corresponding poor counting statistics, the σ^{207}At/σ^{211}At points might more properly be viewed as upper limits.

For the purpose of subtracting secondary yields from the experimental total astatine production cross sections measured in this work, the uncertainties of calculated values were estimated from the corrected data of Li et al.[41] (Figure 10). The relative cross sections for ^{210}At, ^{209}At and ^{208}At at all proton energies were averaged and the percentage difference

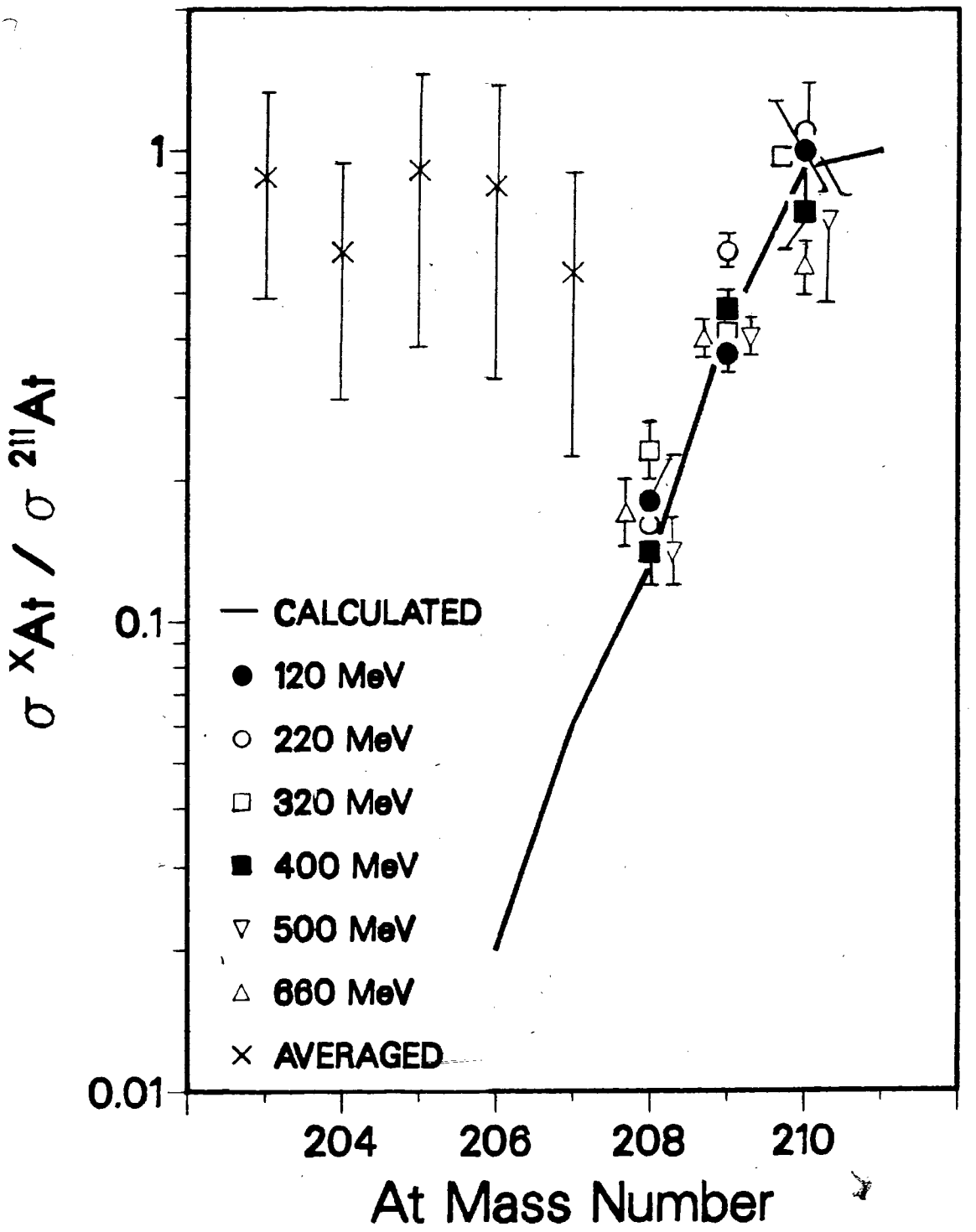

Figure 11 Calculated Secondary Ratios Compared to the Corrected Experimental Data of Ref. 41

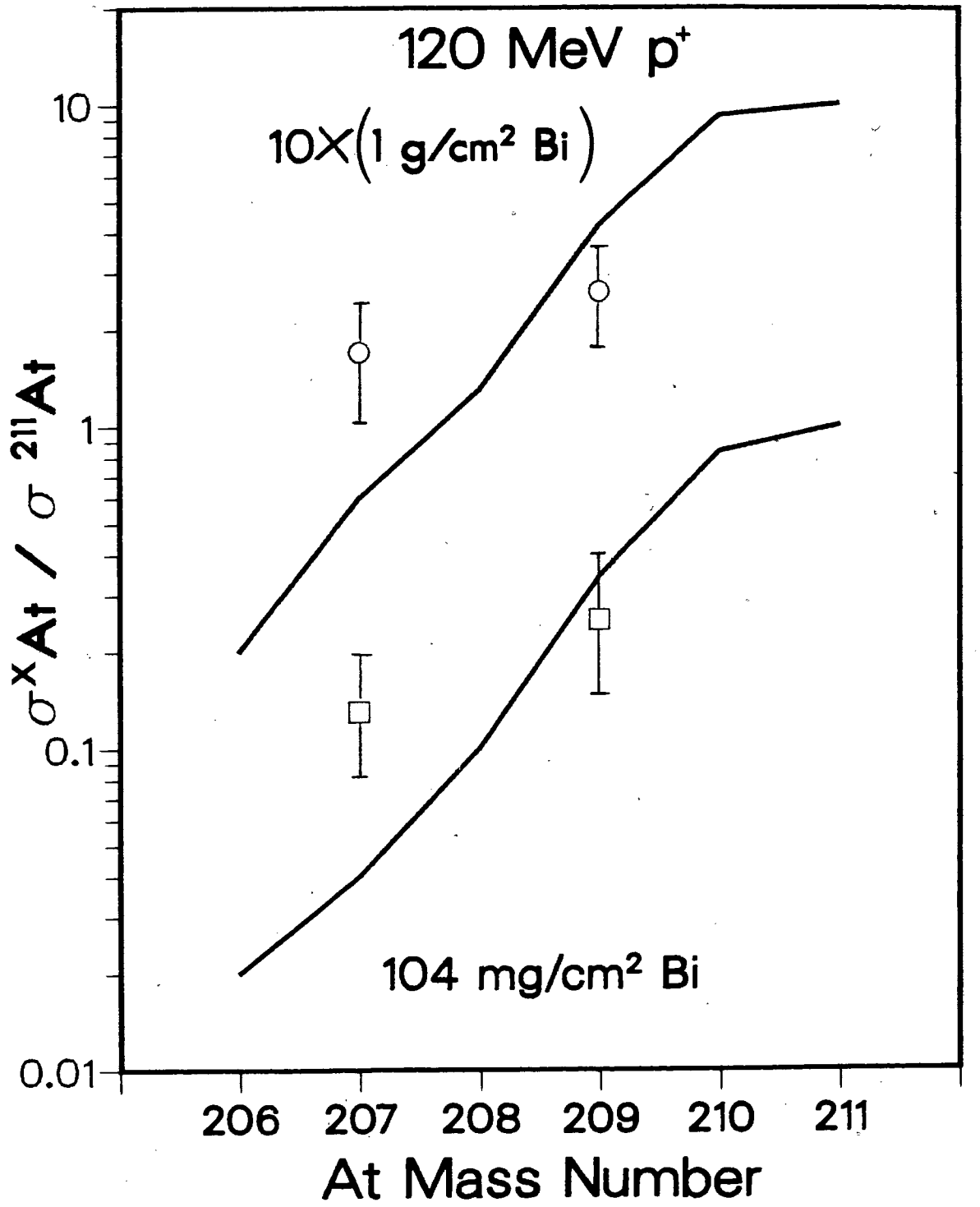

Figure 12 Comparison of Secondary Calculations to IUCF Thick Target Results

from the calculated values taken as a relative error for the calculation. The relative error for $\sigma^{207}At/\sigma^{211}At$ was estimated as an average of the three heavier nuclide errors. The estimated errors are given in Table XI.

Table XI

Estimated Errors for Relative Secondary Yield Calculations

$\frac{\sigma^{210}At}{\sigma^{211}At}$	±3%
$\frac{\sigma^{209}At}{\sigma^{211}At}$	±5%
$\frac{\sigma^{208}At}{\sigma^{211}At}$	±31%
$\frac{\sigma^{207}At}{\sigma^{211}At}$	±13%

RESULTS AND DISCUSSION

Experimental Results

The results of the cross section measurements are presented in Table XII. The cross sections for direct ^{211}At production are labelled $\sigma_{eff}(^{211}At)$ and displayed in the third column. These cross sections are also displayed graphically, as a function of proton energy, in Figure 13. The TRIUMF thin target data can be fit with a linear expression

$$\sigma_{^{211}At}(\mu b) = m \cdot E_p(MeV) + b \qquad (20)$$

$$m = 4.37 \times 10^{-3} \pm 8.31 \times 10^{-4}$$

$$b = 0.316 \pm 0.240$$

However, the 800 MeV point does not fall on this line. The enhancement of ^{211}At production in the LAMPF runs can be attributed to the difference in irradiation methods. At TRIUMF, all irradiations were performed in vacuum, while at LAMPF the targets were in air. Production of alpha and ^{3}He fragments in the air upstream of the target (that subsequently impinged on the target) appears to have significantly increased the secondary production of astatine nuclides. The LAMPF series of cross section determinations is summarized in Table XIII and Table XIV.

As described earlier, the cross section for a specific $(p,\pi^{-}xn)$ reaction is obtained by taking the product of $\sigma_{eff}(^{211}At)$ and the corresponding ratio σ_x/σ_{211}. The values of the cross sections thus obtained for the four heaviest astatines are given in Figure 14 and Table XV. The open circles are the values calculated from the IUCF thick target runs. The solid circles are from measurements of thin targets at TRIUMF and LAMPF. The solid line in each plot represents a smoothed value of the

Table XII

TRIUMF Cross Section Ratio Summary

E_p (MeV)	Target Thickness (mg/cm^2 ±6%)	$\sigma_{eff}(^{211}At)$ (μb)	$\frac{\sigma_{210}}{\sigma_{211}}$	$\frac{\sigma_{209}}{\sigma_{211}}$	$\frac{\sigma_{208}}{\sigma_{211}}$	$\frac{\sigma_{207}}{\sigma_{211}}$	$\frac{\sigma_{206}}{\sigma_{211}}$	$\frac{\sigma_{205}}{\sigma_{211}}$	$\frac{\sigma_{204}}{\sigma_{211}}$	$\frac{\sigma_{203}}{\sigma_{211}}$
120[a]	1000	6.0 ±1.5	-	0.3 ±0.1	-	0.2 ±0.1	-	-	-	-
120[a]	104	5.0 ±1.0	-	0.3 ±0.1	-	0.1 ±0.05	-	-	-	-
160[a]	46.1	4.6 ±0.9	-	0.9 ±0.3	-	1.0 ±0.3	-	-	-	-
180[a]	28.6	2.5 ±0.5	-	2.0 ±0.6	-	4.2 ±1.3	-	-	-	-
188	1.01	1.3 ±0.2	<2	6.2 ±0.7	9.7 ±1.5	20.0 ±2.0	17.0 ±3.0	-	-	-
200[a]	36.2	3.9 ±0.8	-	0.4 ±0.1	-	4.5 ±1.4	-	-	-	-
210	0.94	1.2 ±0.1	1.6 ±0.2	2.7 ±0.1	6.4 ±0.9	16.0 ±0.6	29.0 ±2.0	52 ±4	19.0-±3.0	0.9 ±0.4
214[a]	8.8	1.3 ±0.4	-	0.8 ±0.3	-	7.7 ±3.2	-	-	-	-
225	1.10	1.1 ±0.1	0.7 ±0.2	1.5 ±0.1	2.9 ±0.4	7.9 ±0.3	15.0 ±1.0	39 ±3	20.0 ±4.0	12.0 ±3.0
252	1.13	1.5 ±0.2	0.6 ±0.1	1.1 ±0.1	2.2 ±0.4	6.0 ±0.3	15.0 ±1.0	34 ±4	20.0 ±4.0	32.0 ±5.0
300[b]	1.04	1.4 ±0.4	1.0 ±0.3	0.8 ±0.1	1.8 ±0.3	4.3 ±0.2	10.0 ±1.0	26 ±3	28.0 ±9.0	14.0 ±6.0
350	1.18	2.4 ±0.3	-	1.1 ±0.1	1.9 ±0.5	2.3 ±0.2	7.0 ±1.0	13 ±2	11.0 ±3.0	12.0 ±3.0
399	0.84	2.0 ±0.2	0.5 ±0.2	0.6 ±0.1	1.1 ±0.4	2.2 ±0.2	5.2 ±0.7	16 ±2	7.2 ±3.3	18.0 ±5.0
450	1.04	1.9 ±0.2	0.6 ±0.2	0.5 ±0.1	1.0 ±0.3	1.4 ±0.1	5.0 ±0.8	10 ±1	-	13.0 ±3.0
481	0.77	2.8 ±0.3	0.7 ±0.2	0.5 ±0.1	0.9 ±0.3	1.3 ±0.1	3.1 ±0.4	9 ±1	8.4 ±2.4	11.0 ±2.0

[a] IUCF runs.

[b] Average of 2 runs.

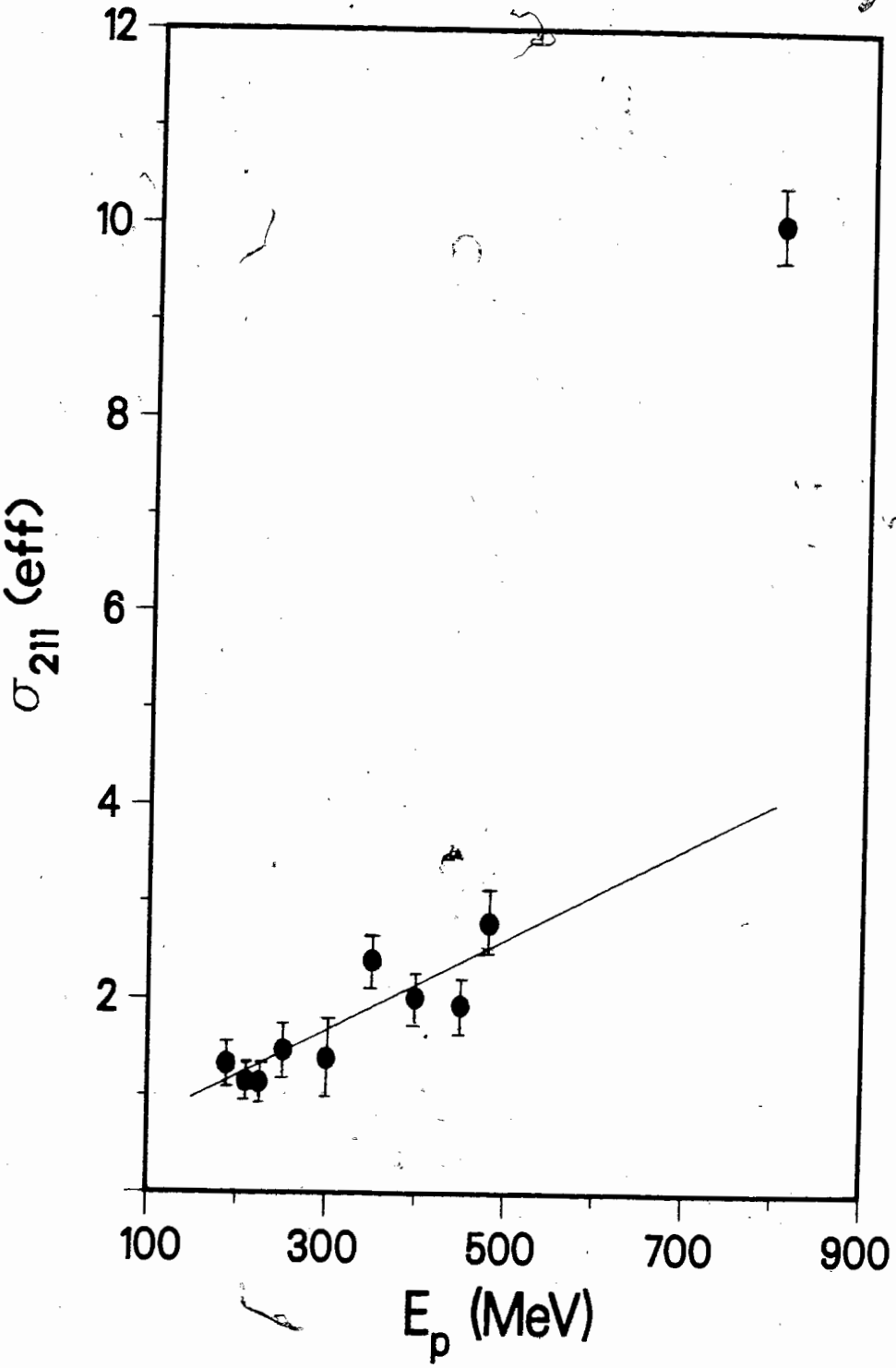

Figure 13 Thin Target ^{211}At Production Cross Sections

Table XIII

LAMPF Direct Target Cross Section Summary

Target	Thickness (mg/cm^2)	$^{*}\sigma_{211}{}_{At}$ (eff) (μb)
At-2	1.76	7.9 ±1.1
At-3	2.00	9.9 ±0.9
At-6d	1.07	10.3 ±0.6
At-7d	0.56	9.7 ±0.6
At-10d	0.34	12.0 ±1.5
At-11	0.69	9.9 ±1.3
At-12	0.71	10.2 ±1.3
		Average = 10.0 ±0.4

Table XIV

LAMPF Cross Section Ratio Summary

Target	Thickness (mg/cm^2)	$\frac{\sigma_{210}}{\sigma_{211}}$	$\frac{\sigma_{209}}{\sigma_{211}}$	$\frac{\sigma_{208}}{\sigma_{211}}$	$\frac{\sigma_{207}}{\sigma_{211}}$	$\frac{\sigma_{206}}{\sigma_{211}}$	$\frac{\sigma_{205}}{\sigma_{211}}$	$\frac{\sigma_{204}}{\sigma_{211}}$	$\frac{\sigma_{203}}{\sigma_{211}}$
At-2	1.76	-	0.8 ±0.3	-	0.5 ±0.2	-	-	-	-
At-3	2.00	-	0.3 ±0.1	-	0.4 ±0.1	-	-	-	-
At-4	2.30	-	0.4 ±0.04	-	0.5 ±0.04	-	1.6 ±0.5	-	-
At-5	2.32	0.9 ±0.2	0.5 ±0.04	0.4 ±0.1	0.5 ±0.02	0.8 ±0.1	2.3 ±0.2	1.9 ±0.3	3.4 ±0.4
At-6	0.72	0.6 ±0.1	0.4 ±0.02	0.5 ±0.04	0.6 ±0.03	0.8 ±0.03	2.7 ±0.3	2.3 ±0.5	2.4 ±0.4
At-7	0.71	0.7 ±0.1	0.5 ±0.04	0.4 ±0.04	0.5 ±0.04	0.7 ±0.1	2.3 ±0.3	-	5.0 ±2.4
At-8	40.2	0.6 ±0.1	0.3 ±0.1	0.2 ±0.02	0.3 ±0.02	0.4 ±0.1	0.8 ±0.1	1.0 ±0.3	1.0 ±0.3
At-10	0.34	1.0 ±0.1	0.5 ±0.04	0.6 ±0.1	0.6 ±0.1	1.5 ±0.3	2.9 ±0.4	2.3 ±1.0	2.3 ±0.7
	Average[a]	=0.70 ±0.05	0.44 ±0.01	0.44 ±0.03	0.52 ±0.01	0.77 ±0.03	2.4 ±0.1	2.0 ±0.3	2.9 ±0.3

[a] The average values are weighted averages of all targets except At-8.

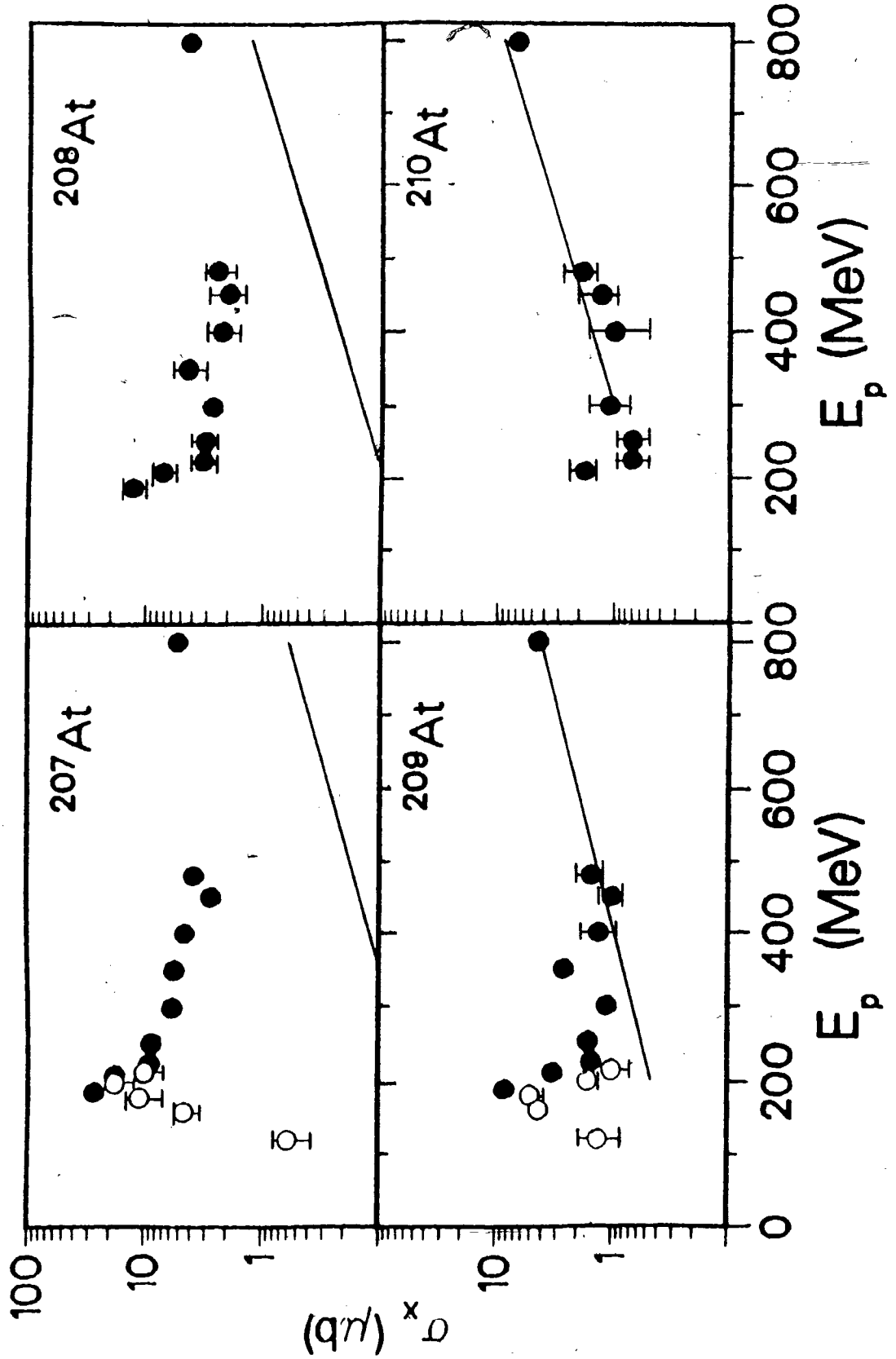

Figure 14 Raw Cross Sections for Heavy Astatine Production. Open circles are IUCF thick target results; the solid line represents secondary contributions.

Table XV

Total Production Cross Sections for Heavy At Nuclides
(including secondary reaction contributions)

E_p (MeV)	σ_{210} (μb)	σ_{209} (μb)	σ_{208} (μb)	σ_{207} (μb)
120_{1000}	-	1.6 ±0.4	-	1.0 ±0.2
120_{104}	-	1.3 ±0.5	-	0.6 ±0.2
160	-	4.2 ±0.8	-	4.6 ±0.9
180	-	5.0 ±1.1	-	11 ±3
188	<2.6	8.1 ±1.5	13 ±3	26 ±5
200	-	1.6 ±0.3	-	17 ±4
210	1.9 ±0.3	3.2 ±0.3	7.7 ±1.3	19 ±2
214	-	1.0 ±0.3	-	10 ±3
225	0.8 ±0.2	1.7 ±0.2	3.2 ±0.5	8.7 ±0.9
252	0.9 ±0.2	1.7 +0.3	3.3 ±0.7	9.0 ±1.3
300	1.4 ±0.6	1.1 ±0.4	2.5 ±0.8	6.0 ±1.7
350	-	2.6 ±0.4	4.6 ±1.3	5.5 ±0.8
399	1.0 ±0.4	1.2 ±0.2	2.2 ±0.8	4.4 ±0.6
450	1.1 ±0.4	1.0 ±0.2	1.9 ±0.6	2.7 ±0.3
481	2.0 ±0.6	1.4 ±0.3	2.5 ±0.9	3.6 ±0.5
800	7.0 ±0.3	4.4 ±0.2	4.4 ±0.3	5.2 ±0.2

calculated contribution to the cross section from secondary reactions for thin targets. The actual secondary contributions used are listed in Table XVI. These were subtracted from the values of Table XV to give final (p,π^-xn) cross sections. For the four lightest isotopes (^{206}At-^{203}At), the contributions from secondary reactions were calculated as negligible. The final astatine (p,π^-xn) excitation functions corrected for secondaries are displayed in Figures 15 and 16 and listed in Table XVII. The open squares are the values measured by Clark et al.[20]. The dashed curves are the calculated predictions of Gibbs[21]. In each case, the reaction threshold is indicated by an arrow. Unfortunately, neither the present measurements nor that of Clark et al.[20] managed to get much information on the coherent reaction ^{209}Bi$(p,\pi^-)^{210}$At. Only one point, at 210 MeV, has a value sufficiently large to exclude formation by secondary reactions. For the other proton energies, only upper limits are displayed. The upper limits were obtained from the difference of the calculated secondary production cross sections and the maximum ^{210}At total production cross section allowed by experimental uncertainties. Also displayed on the ^{210}At plot is a solid curve corresponding to the ^{209}Bi$(p,\pi^0)^{210}$Po excitation function.

The measured individual cross sections (hereafter referred to as σ_x) were summed for each bombarding energy E_p to yield the observed summed cross section $\sum^{x}\sigma_x$. This summed cross section is not the total sum of all (p,π^-xn) cross sections (henceforth called σ_T) since nuclides lighter than ^{203}At have not been included. In order to estimate σ_T, the mass yield distributions of astatine nuclides were assumed to have a Gaussian shape. The astatine cross sections (σ_x), as a function of astatine mass, were fit by least squares to a Gaussian shape at each proton energy above

Table XVI

Summed Calculated Secondary Cross Sections for

(α,xn) and (^{3}He,xn) Reactions

E_p (MeV)	t ±6% (mg/cm^2)	σ_{210}At ±3% (μb)	σ_{209}At ±5% (μb)	σ_{208}At ±31% (μb)	σ_{207}At ±13% (μb)	σ_{206}At (μb)
120	1000	5.5	2.5	0.8	0.30	0.10
120	104	4.2	1.7	0.5	0.20	0.08
160	46.1	3.7	1.5	0.4	0.20	0.06
180	28.6	2.0	0.8	0.2	0.10	0.03
200	36.2	3.1	1.5	0.3	0.10	0.05
214	8.8	1.0	0.4	0.1	0.04	0.01
188	1.01	1.0	0.4	0.1	0.04	0.01
210	0.94	0.9	0.3	0.1	0.04	0.01
225	1.10	0.9	0.3	0.1	0.04	0.01
252	1.13	1.1	0.4	0.1	0.04	0.01
300	1.04	1.1	0.4	0.1	0.05	0.02
350	1.18	1.8	0.7	0.2	0.08	0.03
399	0.84	1.5	0.6	0.2	0.07	0.03
450	1.04	1.5	0.6	0.2	0.06	0.03
481	0.77	2.1	0.8	0.2	0.08	0.04
800	-	9.2	4.2	1.3	0.60	0.20

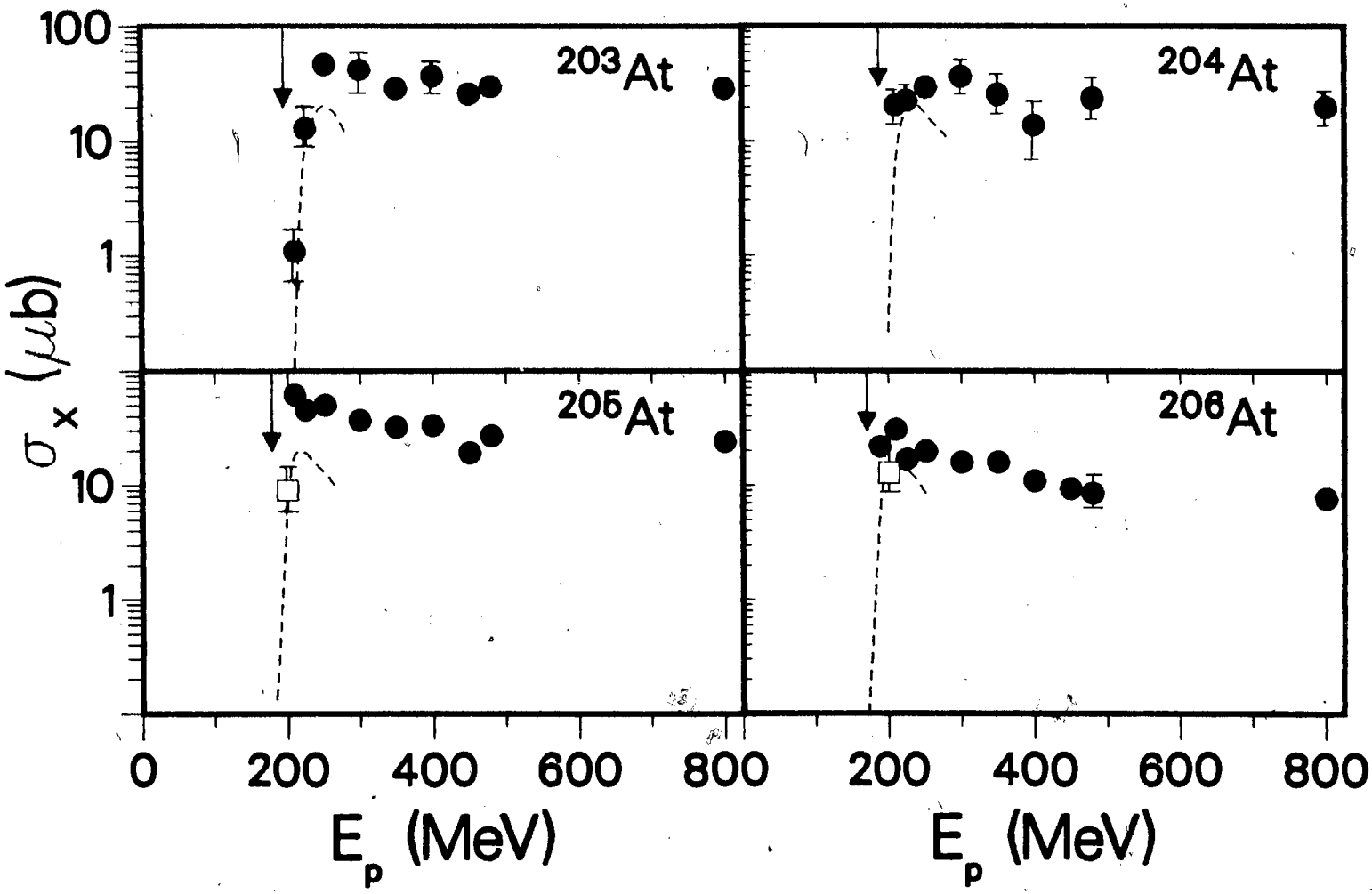

Figure 15 The (p,π^-xn) Excitation Functions Corrected for Secondary Reaction Contributions. Open squares represent results of Ref. 20; dashed curves represent calculated predictions of Ref. 21.

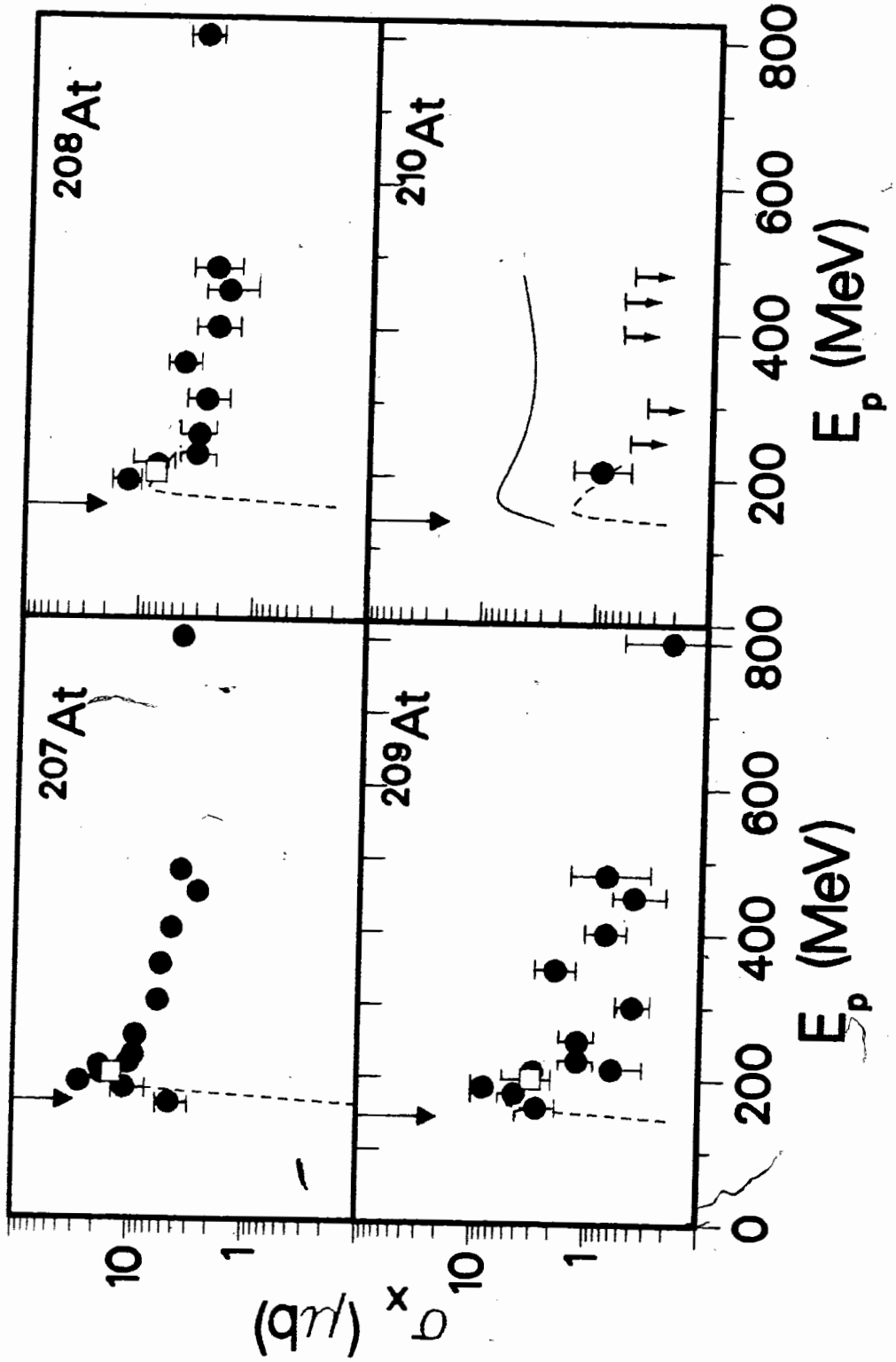

Figure 16 The $(p,\pi^- xn)$ Excitation Functions Corrected for Secondary Reaction Contributions.

The solid curve in the ^{210}At graph shows the (p,π^0) excitation function[19].

Squares and dashed curve as in Fig. 15.

Table XVII

$(p,\pi^- xn)$ Cross Sections for At Production

E_p (MeV)	σ_{210} (μb)	σ_{209} (μb)	σ_{208} (μb)	σ_{207} (μb)	σ_{206} (μb)	σ_{205} (μb)	σ_{204} (μb)	σ_{203} (μb)
160	-	2.7 ±0.8	-	4.4 ±0.9	-	-	-	-
180	-	4.2 ±1.1	-	11 ±3	-	-	-	-
188	-	7.9 ±1.5	13 ±3	27 ±5	22 ±5	-	-	-
200	-	-	-	17 ±4	-	-	-	-
210	0.9 ±0.3	2.9 ±0.3	7.2 ±1.3	18 ±2	35 ±4	62 ± 7	23 ± 4	1.1 ± 0.5
214	-	0.6 ±0.3	-	10 ±3	-	-	-	-
225	-	1.2 ±0.2	3.2 ±0.6	9.1 ±0.9	17 ±2	43 ± 5	22 ± 5	13 ± 4
252	<0.5	1.2 ±0.3	3.1 ±0.7	8.8 ±1.3	23 ±3	51 ± 9	30 ± 7	48 ±10
300	<0.4	0.7 ±0.4	2.7 ±0.8	5.7 ±1.7	14 ±4	36 ±11	39 ±17	20 ±10
350	-	1.9 ±0.4	4.3 ±1.4	5.4 ±0.8	17 ±3	31 ± 6	26 ± 8	29 ± 8
399	<0.6	0.6 ±0.2	2.2 ±0.8	4.4 ±0.6	10 ±2	32 ± 5	14 ± 7	36 ±11
450	<0.6	0.4 ±0.2	1.8 ±0.7	2.6 ±0.3	9.5 ±1.8	19 ± 3	-	25 ± 6
481	<0.5	0.6 ±0.3	2.3 ±0.9	3.7 ±0.5	8.7 ±1.5	25 ± 4	24 ± 7	31 ± 7
800	-	0.2 ±0.3	3.1 ±0.5	3.9 ±0.2	7.7 ±0.4	24 ± 2	20 ± 3	29 ± 3

252 MeV. Below 252 MeV, the lighter astatines ($\leq^{202}$At) are not expected to be produced in significant quantities and σ_T was simply approximated by $\sum^{x}\sigma_x$. The parameters of the Gaussian fits are summarized in Table XVIII. The mean number of neutrons ($\bar{x}$) corresponding to formation of the $^{210-x}$At products is given in the second column. The peak of the Gaussian (at mass number 210-$\bar{x}$) and the full width at half maximum (FWHM) of the Gaussian are given in the third and fourth columns. The final column shows values of $\bar{x}$ for the series of reactions ^{209}Bi(p,xn)$^{209-x}$Po, x = 0-14[34], for comparison. A typical mass distribution and corresponding Gaussian for E_p = 481 MeV are displayed in Figure 17. The upper limits of ^{202}At, ^{201}At and ^{200}At are also displayed. Their values are in keeping with the assumption of a Gaussian mass distribution. The Gaussian fits were then used to generate σ_T, estimated by summing over At masses. Table XIX shows the estimated values of σ_T as well as the experimental sums $\sum^{x}\sigma_x$. The quoted errors in σ_T are probably overestimated since the uncertainties in $\bar{x}$, σ_{max} and FWHM were treated as independent; however, the lower limit of σ_T was never taken as lower than the measured $\sum^{x}\sigma_x$. Figure 18 shows the estimated σ_T values as solid circles. Also included are the total inclusive cross sections (σ_{inc}) from Cochran et al.[8] (triangle), Crawford et al.[7] (open circle) and DiGiacomo et al.[9] (crosses). The solid and dashed lines represent the calculated values of Long et al.[22] and Gibbs[21], respectively. As before, the open square is from Clark et al.[20].

The data presented contain three elements that can be used in attempts to understand the (p,π) process: the individual (p,π^-xn) excitation functions $\sigma_x(E_p)$, the total (p,π^-xn) cross section (σ_T) and the average number of nucleons emitted from the residual nucleus ($\bar{x}$). These elements

Table XVIII

Gaussian Fit Parameters of At Mass Distributions

E_p (MeV)	$\bar{x}$	σ_{max} (μb)	FWHM (units of A)	$\bar{x}_{(p,xn)}$[b]
188	2.8 ±0.4	-	-	-
200[a]	3.4 ±0.6	-	-	-
210	4.4 ±0.3	-	-	6.0 ±0.2
225	4.9 ±0.6	-	-	-
252	6.3 ±1.0	43.2 ±8.2	4.8 ±4.3	-
300	6.4 ±0.4	42.6 ±3.2	4.3 ±1.5	5.4 ±0.1
350	6.0 ±0.4	31.1 ±3.5	4.3 ±1.9	-
399	6.1 ±0.8	47.3 ±3.8	3.0 ±0.6	5.6 ±0.1
450	6.4 ±0.1	27.6 ±1.1	3.9 ±0.6	6.1 ±0.2
481	6.5 ±0.6	29.6 ±3.5	4.3 ±2.5	6.3 ±0.1
800	7.2 ±1.5	27.8 ±5.4	5.4 ±4.8	-

[a] Ref. 20.

[b] Ref. 34.

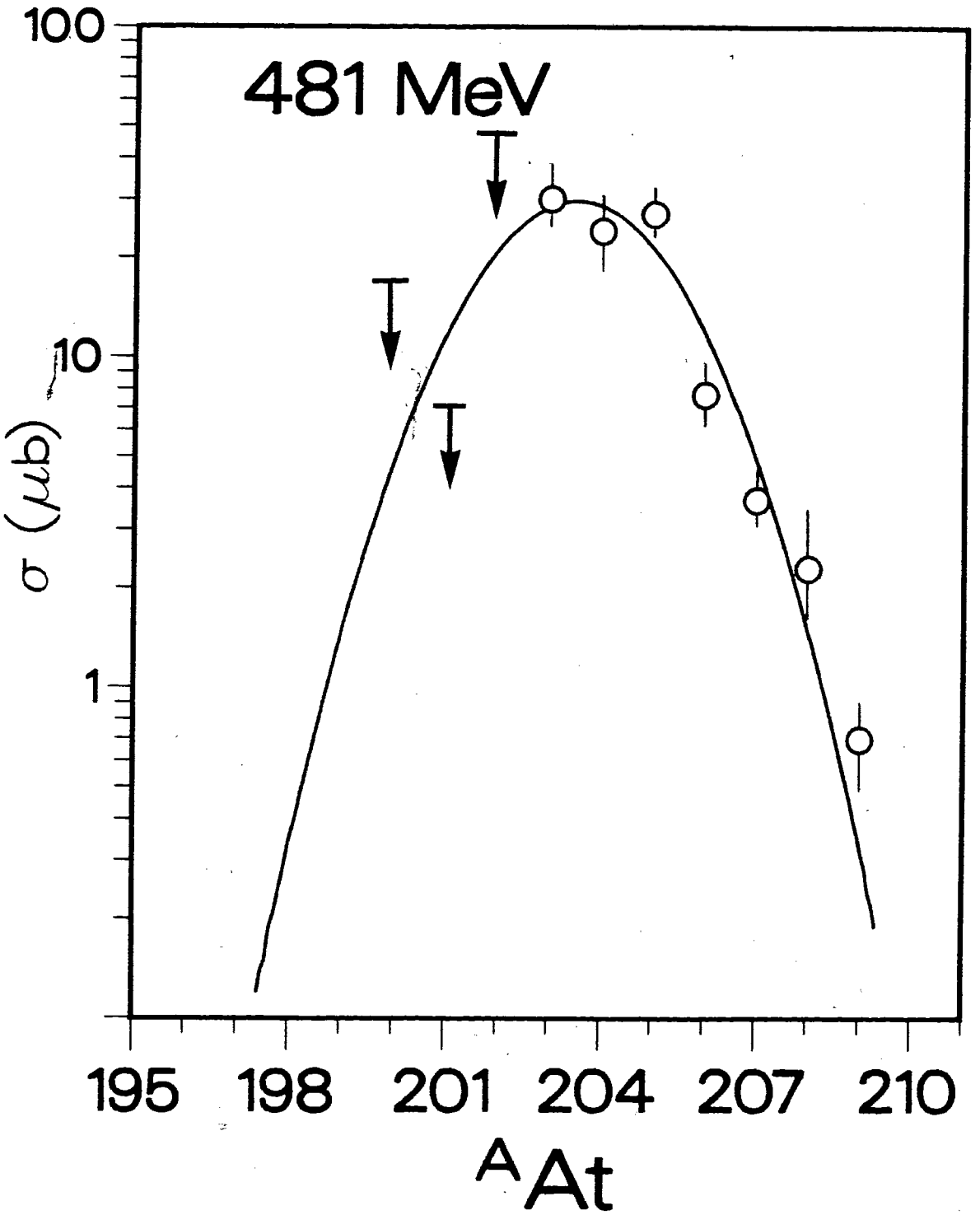

Figure 17 Residual Astatine Mass Distribution at E_p = 481 MeV.

The line is a Gaussian fit.

Table XIX

Summed and Estimated Total Cross Sections for $(p,\pi^- xn)$

E_p (MeV)	$\Sigma\sigma_x$ (μb)	σ_t (estimated) (μb)
188	70 ±9	-
200[a]	48 ±13	-
210	143 ±10	-
225	112 ±10	-
252	160 ±14	220^{+203}_{-74}
300	141 ±23	195^{+72}_{-72}
350	115 ±13	145^{+67}_{-43}
399	102 ±13	150^{+32}_{-32}
450	≈80	115^{+18}_{-18}
481	116 ±11	135^{+82}_{-30}
800	89 ±5	160^{+147}_{-76}

[a] Reference 20.

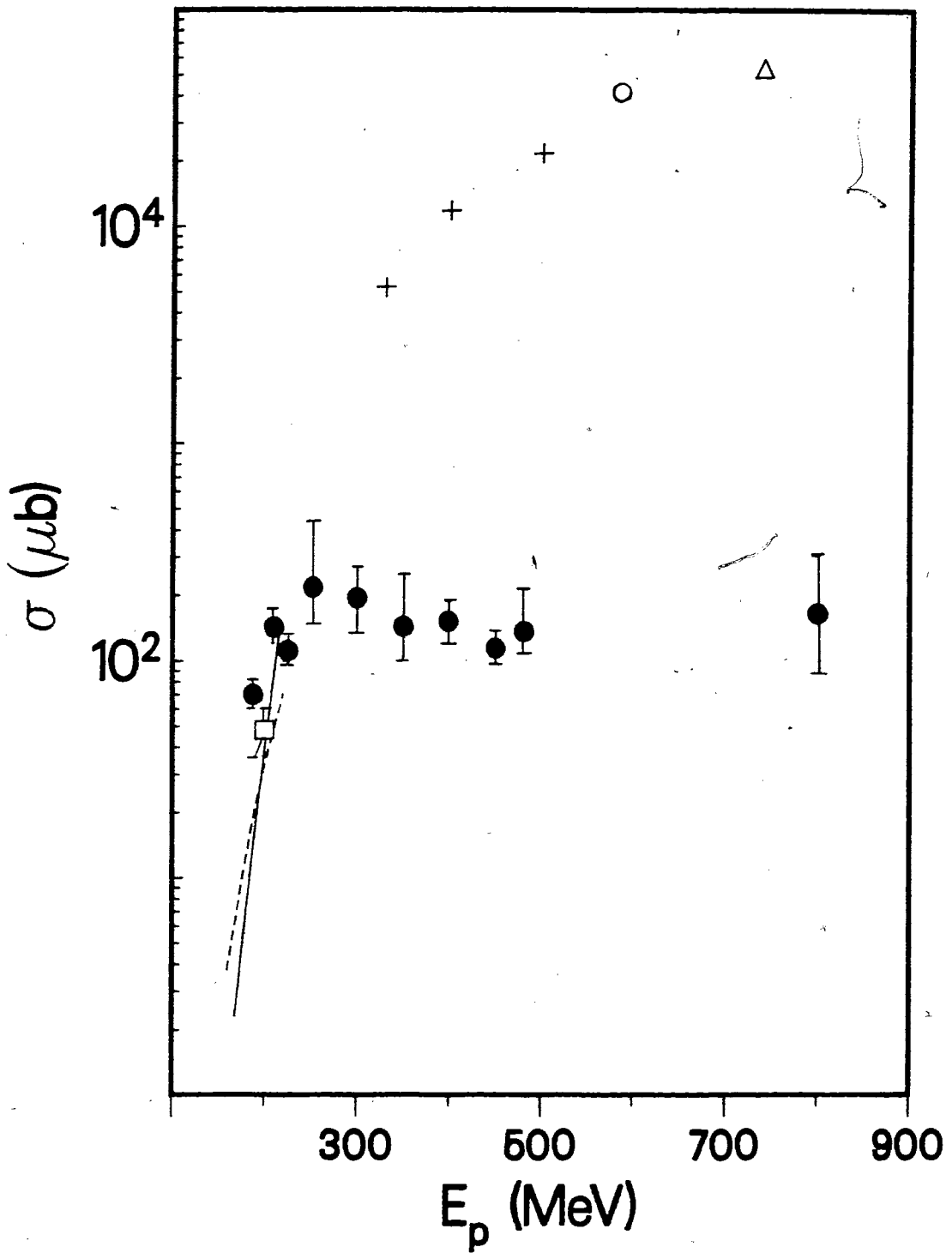

Figure 18 Summed (p,π^-) Cross Sections. Square: Ref. 20; crosses: Ref. 9; triangle: Ref. 8; open circle: Ref. 7; solid line: Ref. 22; dashed line: Ref. 21.

can be related to other experimental data and calculations in an attempt to understand the underlying causes of the observed data.

The (p,π^-xn) Excitation Functions

The excitation functions displayed in Figures 15 and 16 generally exhibit a similar energy dependence. All σ_x rise steeply immediately after threshold, reaching a maximum within 50 MeV. However, the value of the maximum cross section increases dramatically from $\leq\approx 2$ μb for x = 0 (^{210}At) to ≈50 μb for x = 5-7 ($^{205-203}$At). Beyond the maximum cross section, all σ_x decrease with increasing E_p, though the relative rate of decrease is different. For x = 1, the decrease is rapid, giving rise to an apparent peak in the excitation function. The rate of decrease diminishes with increasing x, resulting in the disappearance of the peak at x ≈ 6. It is unlikely that the apparent peak is caused by a resonance. A simpler explanation may lie in the relative magnitudes of a specific σ_x and its neighbours $\sigma_{(x+1)}$, $\sigma_{(x+2)}$, etc. For low values of x, $\sigma_{(x+1)}/\sigma_x$ is high and the opening of a new, relatively stronger reaction channel (the (x+1) channel), as well as the following channels, causes a steep decrease in the σ_x excitation function resulting in an apparent peak. For greater x, the relative magnitude of $\sigma_{(x+1)}/\sigma_x$ is smaller and the opening of the (x+1) channel has less effect on σ_x. Thus, the apparent peak above threshold grows weaker and finally disappears as $\sigma_{(x+1)}/\sigma_x$ decreases. The generally smooth shapes of σ_x for x = 6, 7 are then also consistent with the prediction that the (p,π^-xn) cross sections leading to nuclides lighter than ^{203}At follow the Gaussian distribution assumed in calculating σ_T. The excitation functions for (p,π^-xn) display similar shapes and energy dependences to those of the $^{127}I(\pi^-,\pi^-xn)^{127-x}I$, x = 1-10, series

of reactions measured by Ohkubo et al.[57]. The shapes of the iodine excitation functions were deemed to result from cascade-evaporation mechanisms in which the residual nucleus de-excites by emission of neutrons. The similarity between the (p,π^-xn) and (π^-,π^-xn) excitation functions suggest that the excitation function shapes of the present work are determined most probably by the nucleus de-excitation mechanism and not by the pion production step.

Figures 15 and 16 display the results of two other experimental measurements. The first is the measurement of (p,π^-xn) at 200 MeV by Clark et al.[20] (open squares). The present work is in excellent agreement with the 200 MeV data. The second experimental measurement displayed is the $^{209}Bi(p,\pi^0)^{210}Po$ excitation function from Ward et al.[19]. This is shown as a continuous solid line in the ^{210}At plot of Figure 15. While no direct comparison with the (p,π^-) excitation function can be made, the shape of the (p,π^0) curve is generally similar to those of the (p,π^-xn) reactions. Both display a sharp rise after threshold with an apparent peak and subsequent decrease in cross section. Unfortunately, no data on (p,π^0xn) reactions exist. The products measured by radiochemical methods[34] are the $^{209-x}Po$ activities due mainly to (p,xn) reactions which have a much larger cross section than that of (p,π^0xn). Though the coherent (p,π^-) excitation function could not be measured, the upper limits on that particular σ_x show that the (p,π^0) reaction on ^{209}Bi is roughly one order of magnitude larger. This is not surprising when the elementary pion production processes are considered. A neutral pion can be produced by the following nucleon-nucleon reactions:

$$p + p \rightarrow p + p + \pi^0 \qquad (21a)$$

$$p + n \rightarrow p + n + \pi^0 \qquad (21b)$$

$$p + n \rightarrow d + \pi^0 \qquad (21c)$$

A negative pion can only be produced in the reaction:

$$p + n \rightarrow p + p + \pi^- \qquad (22)$$

The ratio of cross sections for Reactions 21b and 22 has been measured by Rushbrooke *et al.*[58]. Using a broad spectrum of neutron energies up to 970 MeV, incident on a hydrogen bubble chamber, the measured ratio was

$$\frac{\sigma(np \rightarrow np\pi^0)}{\sigma(np \rightarrow pp\pi^-)} = 2.67 \pm 0.43$$

The cross section for Reaction 21a is of the same order as that of 22, while that of 21c is expected to be about the same magnitude from the application of charge independence to the $p + p \rightarrow \pi^+ + d$ reaction[59]. As well as being produced in initial N-N interactions, pions produced in a nucleus can charge exchange on their way out of the nucleus. Here again, more neutral pions can be produced by the reactions:

$$n + \pi^+ \rightarrow p + \pi^0 \qquad (23a)$$

$$p + \pi^- \rightarrow n + \pi^0 \qquad (23b)$$

while negative pions are produced only by:

$$n + \pi^0 \rightarrow p + \pi^- \qquad (24)$$

While no attempt was made to calculate the relative magnitude of π^0 and π^- production for bismuth, it is clear from qualitative considerations that an order of magnitude difference between (p,π^-) and (p,π^0) is not precluded.

Finally, with regard to the individual excitation functions, there are the calculations of Gibbs[21]. These are shown as dashed curves in the individual σ_x plots. The agreement between calculated and experimental values is very good for x = 0-3. For values of x > 4, the calculated excitation functions underestimate the experimental data by significant amounts. In order to understand the difference between predicted and observed values, the model used by Gibbs must be examined. The calculation used an optical model Distorted Wave Impulse Approximation (DWIA). Pion production was assumed to result only from target emission. That is, the pion was produced in a collision of the incoming proton with a target nucleon. Production by projectile emission of a π^0 that subsequently charge exchanges to a π^- was ignored. Other mechanisms which Gibbs called "exotic" (such as Δ^{++} formation) were also ignored. A second assumption in this model is that the (p,π^-) cross section to a given nuclear state can be represented by a cross section to a typical nuclear state. While this assumption would not be valid for light nuclei, it is appropriate for a heavy nucleus such as ^{209}Bi, where the spacing of nuclear states is close. Based on these assumptions, Gibbs calculated the cross section to a 2-particle 1-hole state described by the configuration

$$\{[1h_{9/2}^{-1}\ 2g_{9/2}]_0 \times 2g_{9/2}\}_{9/2}$$

as a function of the excitation energy of the residual nucleus (or, conversely, the pion final energy). To obtain the total cross section for a particular excitation energy, the cross section to the typical state is multiplied by the level density for that excitation energy. The cross section to ^{210}At, the coherent (p,π^-) product, is obtained by integrating over

the first 10 MeV of excitation energy. Cross sections for lighter nuclides are obtained by allowing for neutron evaporation at higher excitation energies. The predicted astatine mass distribution and σ_x cross sections were in very good agreement with the data of Clark et al.[20] at 200 MeV. While the model continues to account for σ_x for the heavier astatines ($\geq\approx^{207}$At) up to $E_p \approx 250$ MeV, it fails to predict the correct σ_x for lighter nuclides. This disagreement can be explained by examining two aspects of the Gibbs model.

The first aspect concerns the assumption that only target emission of the pion takes place. It may well be that, while this assumption holds true for the production of heavier astatines, the lighter nuclide production is due to both target emission and projectile emission (π^0 followed by charge exchange to π^-). In this case, the model simply fails, as no account of charge exchange is included. Gibbs himself refers to target-only emission as "admittedly an extreme point of view"[21]. If this is indeed the case, then the difference between the observed values of σ_x and the calculated values is due to the fraction of σ_x produced by charge exchange mechanisms.

A second aspect of the model can account for the discrepancies in calculated and observed values without a resulting breakdown of the model. Since the pion production relies on the nucleus being left in "typical" 2plh states, the cross section is sensitive to the number of available "typical" states; that is, the level density of 2plh states. Gibbs used a level density parameter given by:

$$\rho(E) = 0.004\ (E + 15)^2\ \text{MeV}^{-1} \qquad (25)$$

where E ≡ excitation energy in MeV. A two-nucleon model calculation for the corresponding $^{209}Bi(p,\pi^0)^{210}Po$ reaction[19] found that the cross section was quite sensitive to the level density of ^{210}Po states. In that case, a satisfactory fit to the data was obtained using a density parameter given by the form:

$$\rho(E) \alpha \exp\{2(aE)^{1/2}\} \qquad (26)$$

where a is a parameter dependent on nuclear mass number (in units of MeV^{-1}).

The level density in Equation 26 generally refers to all states, not just the 2p1h states. However, Equation 26 is clearly a faster rising function of E than Equation 25. If the level density in Gibbs' model was replaced by a function with a steeper dependence on E (perhaps a E^3 dependence), sufficiently high cross sections might be attained for σ_x, where x = 4-7. If this proved to be the case, σ_x for the (p,π^-xn) reactions could be accounted for entirely by target emission.

Before ending the discussion of the individual excitation functions, a brief note must be made of the slightly higher values of σ_x at 350 MeV for the ^{209}At and ^{208}At products. In light of recent claims of the observance of a dibaryon resonance in the (p,π) reaction on copper at E_p = 350 MeV[10,11], it should be noted that the higher values in the case of ^{209}At and ^{208}At are due simply to fluctuations in the value of $\sigma_{eff}(^{211}At)$ (see Figure 13). If smoothed values of $\sigma_{eff}(^{211}At)$ are used (Equation 20), no peak in σ_x at 350 MeV is observed.

The Astatine Mass Distributions

The residual astatine mass distributions above a proton energy of

252 MeV can be described by the Gaussian shapes summarized in Table XV. The most probable At mass is ^{204}At, corresponding to an average emission of ≈6 neutrons. Below 252 MeV, the most probable number of emitted neutrons ($\overline{x}$) is rapidly increasing as successive (p,π^-xn) reaction channels become available with increasing energy. The relatively constant value of $\overline{x}$ from 252 MeV to 800 MeV for the (p,π^-xn) reactions is also found for the ^{209}Bi(p,xn) reactions over the energy interval 210-481 MeV[34]. The (p,xn) process is thought to involve an emission of a fast neutron from an initial pn → np charge exchange interaction, followed by a subsequent evaporation of (on average) 5 neutrons. The similarity of the Gaussian-shaped residual mass distributions of both astatine (in (p,π^-xn)) and polonium (in (p,xn)) nuclei suggest a similar reaction mechanism. An initial emission of a fast particle (a π^- in (p,π^-xn) and a neutron in (p,xn)), followed by evaporation of an average number of neutrons.

The behaviour of $\overline{x}$ as a function of projectile energy can give an indication of the distribution of energies in the (p,π^-xn) reaction channel. If the emitted neutrons are assumed to result from an evaporation mechanism, the energy transfer to the nucleus can be approximated. Taking an average neutron binding energy of ≈8 MeV and adding a small kinetic energy (≈2 MeV per neutron) gives an average energy transfer of:

$$\overline{x} \cdot (\langle B_n \rangle + 2 \text{ MeV}) = 10\overline{x} \text{ MeV} \qquad (27)$$

For the lower proton energies, where $\overline{x}$ is increasing, the energy transfer to the nucleus also increases. For the higher projectile energies, $\overline{x}$ seems to reach an optimal value of 6, corresponding to ≈60 MeV excitation energy for the nucleus. In fact, the excitation energy could be much higher if

some part of it were accounted for by charged particle evaporation. However, with charged particle emission, nuclei other than astatine result and are not detected by the present radiochemical technique. For the case of no charged particle emission, it appears the average energy transfer to the nucleus is approximately 60 MeV in the (p,π^-xn) channel. From considerations of energy conservation, something can be said about the energy of the emitted pion. The total available energy is the proton energy in the centre of mass system. For protons on bismuth, $E_{CM} \approx E_{LAB}$. Assuming an initial pion emission, the total energy of the system just before neutron evaporation can be expressed roughly as:

$$E_p = m_\pi c^2 + E_\pi + E_A + E^* \qquad (28)$$

where E_p, E_π and E_A represent the kinetic energies of the proton, pion and residual nucleus, $m_\pi c^2$ is the rest mass of the pion ($\approx$140 MeV) and E^* is the excitation energy of the residual nucleus. Discounting the relatively small recoil energy (E_A) and approximating E^* with Equation 27 gives an approximation of the pion energy.

$$E_\pi \approx E_p - 140 \text{ MeV} - 10\overline{x} \qquad (29)$$

For the lower values of E_p (and $\overline{x}$), the pion energy is in the range 20-30 MeV and the increase in available energy (E_p) is compensated for mainly by an increase in the nucleus excitation energy, with a subsequent increase in $\overline{x}$. At higher E_p, $\overline{x}$ is practically constant and the pion energy has to increase with increasing E_p in order to conserve energy in the (p,π^-xn) channel. The radiochemical technique of the present work samples two different pion energy regions. Near threshold, where the

probability of charged particle emission is low, the (p,π^-xn) channel accounts for >90% of the total (p,π^-) reaction[20]. Pions with an average of 20-30 MeV energy are emitted and the residual nucleus dissipates the excess energy by neutron evaporation. With increasing incident energy, a near constant average excitation energy is observed and the excess energy is removed by the pion. Here, the radiochemical technique samples increasingly energetic pions produced in the (p,π^-xn) channel at a constant average momentum transfer to the nucleus. The average momentum transfer for the (p,xn) reactions[34] was obtained by the relation

$$\langle p \rangle = \left[\langle E_{SEP} \rangle \cdot (2m_N) \right]^{1/2} \qquad (30)$$

where $\langle E_{SEP} \rangle$ was the average separation energy of the residual nucleus (based on the average $\overline{x}$) and m_N is the nucleon mass. For $\langle E_{SEP} \rangle \approx$ 60 MeV, the average momentum transfer in the (p,π^-xn) reactions above 252 MeV is ≈335 MeV/c. This is similar to the value calculated for (p,xn)[20], ≈350 MeV/c, and consistent with other proton-nucleus measurements at intermediate energy which have examined linear momentum transfer[60,61].

The Total (p,π^-xn) Cross Section

The estimates of the total (p,π^-xn) cross section (σ_T), as calculated from the Gaussian mass distributions, were previously given in Table XVI and Figure 18. Figure 18 also displays experimental determinations of the inclusive cross sections (σ_{inc}) for heavy nuclei, as well as the summed cross sections extrapolated from Gibbs[21]. The solid line in Figure 18 represents the predicted σ_T from the intranuclear cascade calculation (INC) of Long et al.[22]. While both the INC and Gibbs'

calculations reproduce the sharp rise of σ_T from threshold to ≈200 MeV, the magnitudes of the two predictions differ by a factor of two at $E_p \approx$ 220 MeV. The possible reasons for the underestimation of σ_T in the Gibbs model have previously been discussed. In light of the agreement of the INC calculation with the experimental data at proton energies slightly above 200 MeV, the dominant mechanisms of pion production in the INC must be examined.

Long et al.[22] use a simplified version of a full INC type of calculation[62]. In their version of the Monte Carlo cascade code, only the most energetic particle is followed through a series of nucleon-nucleon and nucleon-pion interactions in the nucleus. The other particles resulting from proton scattering, pion production or pion scattering are ignored and assumed to simply "heat up" the residual nucleus. The result obtained by this type of calculation gives only σ_T, the total (p,π^-xn) cross section. As with standard INC codes, the reaction cross section is considered to be some product of individual $NN \rightarrow NN$, $NN \rightarrow NN\pi$ and $\pi N \rightarrow \pi N$ cross sections. The three dominant pion production mechanisms of the calculation are: (1) direct π^- production in an initial proton-neutron collision, $pn \rightarrow pp\pi^-$; (2) proton charge exchange, $pn \rightarrow np$, where a resulting fast neutron subsequently produces the pion in a second collision, e.g. $nn \rightarrow d\pi^-$; (3) neutral pion production in $pp \rightarrow pp\pi^0$ or $pn \rightarrow pn\pi^0$ collisions, followed by π^0 charge exchange, $\pi^0 n \rightarrow \pi^- p$. The energy requirements for pion production in the NN centre of mass are provided by the incident proton energy and the Fermi energy of the bound nucleons. For ^{209}Bi and ≈200 MeV protons, Long et al.[22] estimate that about 8% of the nucleons have sufficient Fermi momenta to exceed the required centre of mass energy. The eventual

value of σ_T is sensitive to the input values of the thresholds for the individual $NN \rightarrow NN_\pi$ cross sections. These thresholds are expressed in terms of η, the maximum pion momentum in the NN_π centre of mass:

$$\eta^2 = \frac{(T - T_o)(T + 2\mu - \mu^2/2m)}{4(1 + T/2m)} \tag{31}$$

$$T = (W_{NN}^2 - 4m^2)/2m \tag{32}$$

$$T_o = 2\mu + \mu^2/2m \tag{33}$$

The notation of Equations 31 to 33 is that of Long et al; μ and m refer to pion and proton rest masses, W_{NN} is the NN centre of mass energy. The energy dependences of the NNπ cross sections (in terms of η) are then used in determining the rate of pion production in the Monte Carlo calculation. Clearly, η (and eventually σ_T) is sensitive to the form of W_{NN}. Long et al., in fact, performed three calculations. In the first, they used a form of W_{NN} described by:

$$W_{NN}^2 = (E + \varepsilon)^2 - (\vec{p} + \vec{k})^2 \tag{34}$$

where $(E,\vec{p})$ and $(\varepsilon,\vec{k})$ refer to proton and bound nucleon energy momenta, respectively. The energy of the bound nucleon was simply taken as its mass, $\varepsilon = m$. This type of calculation produced a value of $\sigma_T = 11.6 \pm 2.5$ μb at $E_p = 200$ MeV. This value underestimates the experimental σ_T by a factor of four. In a second calculation, the struck nucleon was assumed to be "free" at the moment of pion production. Here, $\varepsilon = (m^2 + \vec{k}^2)^{1/2}$ and the calculated value of σ_T was 190 ± 28 μb at $E_p =$ 200 MeV. This value overestimates the experimental data by a factor of four.

In order to balance the extreme results of the first two calculations,

Long et al. assumed a form of W_{NN} somewhere between the two previous forms. This was accomplished by a third calculation that relied on values of η from the two previous results. The average input NN_π cross sections were taken to have a form described by:

$$\overline{\sigma}_{NN_\pi} = \left(\frac{\eta_1}{\eta_2}\right)\sigma_{NN_\pi}(\eta_2) \qquad (35)$$

where the subscripts refer to the earlier calculations and η is described by Equation 31. The third calculation gave a value of $\sigma_T = 42.9 \pm 8.4$ μb at 200 MeV, in good agreement with experiment[20]. This cross section represented 26 π's produced from 30,000 incident protons. Of the total, 10 were produced directly, 12 resulted from nn collisions after an initial pn charge exchange and 4 came from π^0 charge exchange. The simplified INC calculation is in good agreement with the present data to 220 MeV. At higher energies the simplified calculation cannot be applied to $(p,\pi^- xn)$ reactions. When the NN collision energy becomes sufficiently high to permit charged particle emission, a full version of an INC code must be used to follow all scattered particles and extend the calculation to higher incident energies. Since over half of the π's produced in the INC calculation result from mechanisms other than direct $pn \rightarrow pp\pi^-$ production, it is interesting to note that the Gibbs direct production model[21] estimates σ_T at half the value of the INC calculation. However, given the sensitivities of both models to centre of mass energy (Long et al.) or 2p1h level density (Gibbs), it is unclear whether one model should be accepted at the expense of the other.

Both of the calculations discussed previously examine pion production

near threshold. While the excitation functions given by Gibbs[21] can be extrapolated to $E_p \approx 280$ MeV, it is unlikely such an extrapolation would be strictly valid. However, a third type of calculation has been performed by I. Kelson[63]. The calculation examines the behaviour of σ_T relative to σ_{inc} and the behaviour of $\bar{x}$ for the entire energy range of the present work. A schematic model is used (without regard for the specific pion production mechansisms) to explain the energy dependence of both. Before this model is presented, the general features of σ_T and σ_{inc} are reviewed.

Figure 19 again displays the estimated values of σ_T. The energy dependence of σ_{inc} is shown as a solid line. The line is a smooth curve drawn through the previously mentioned experimental data[7-11]. Also shown are experimental determinations of the elementary $n + p \rightarrow p + p + \pi^-$ cross section obtained from neutron measurements[58,59,64-66]. For the purpose of comparison, the np data have been converted to centre of mass energies. Below ≈250 MeV, the similarity of the energy dependence of σ_{inc}, σ_T and σ_{np} is immediately apparent. There can be no doubt that the (p,π^-xn) channel is responsible for most of the inclusive pion production at low energies. Though the similarity of both σ_{inc} and σ_T to σ_{np} could be fortuitous, it can also be argued as indicative of the fact that the direct $p + n \rightarrow p + p + \pi^-$ is the main mechanism of pion production at lower energies. At incident energies about ≈250 MeV, σ_T deviates from σ_{inc} and σ_{np} and levels off with increasing energy. The energy region where σ_T turns over roughly corresponds to a threshold where (after emission of a pion and ≈6 neutrons) a proton has sufficient energy to leave the nucleus. At higher energies, both the incident proton and the proton resulting from π^- production can escape. In either case, the residual

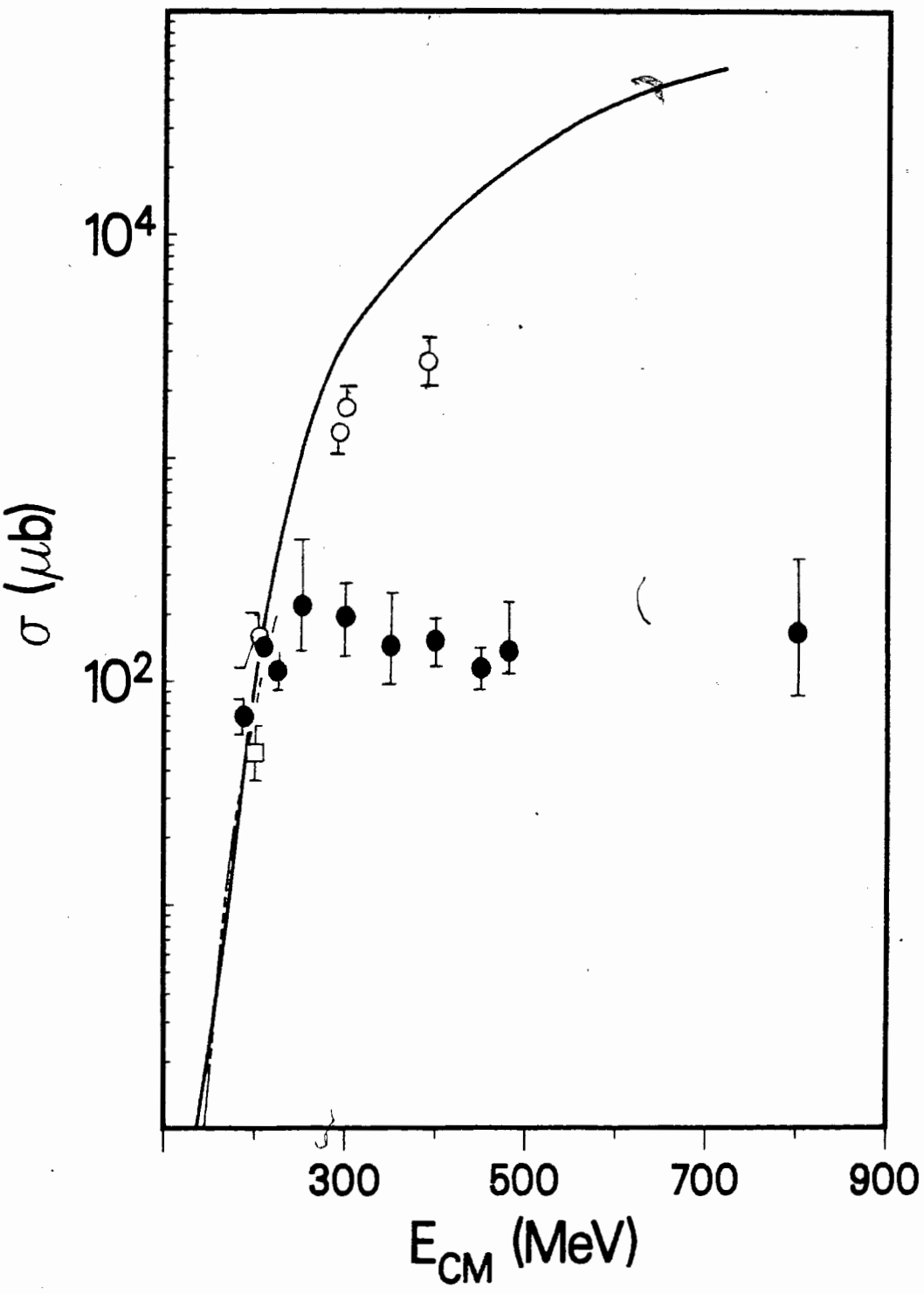

Figure 19 Energy Dependence of Elementary, Summed and Inclusive π^- Cross Sections. Solid line: σ_{inc}; open circles and dashed line: σ_{np} from Refs. 58, 59, 64-66.

nucleus is not astatine and the process is not observed in this experiment. At an energy ≈300 MeV, σ_{np} also levels off while σ_{inc} continues to increase. This energy roughly corresponds to the threshold of double pion production. The continuing increase in σ_{inc} could be due to double pion production or to an increase in pion production by charge exchange mechanisms not available to σ_{np}. If charge exchange is important to σ_{inc}, it will be important to its subset σ_T. From the available data, there is no way of knowing if the high energy behaviour of σ_T is characterized by direct or charge exchange mechanisms.

A Schematic Model Approach

I. Kelson has performed a schematic parametric calculation comparing σ_T to σ_{inc} as a function of incident proton energy[63]. His calculation is discussed in this section. By concentrating only on the ratio σ_T/σ_{inc}, many of the complexities of the pion production mechanism are avoided and a single parameter is used to account for both the cross section ratio and $\bar{x}$ as functions of E_p. The intermediate pion production mechanisms are ignored. No matter how a pion is produced, the final state is assumed to contain a π^- (that escapes after depositing some energy in the nucleus) and two positive energy protons. Kelson treats the nucleus as a single point interaction region, assumes isotropic distributions and averages over all weak energy dependences. The more energy the final-state protons have, the more likely they are to escape the interaction region; that is, the nucleus. The present experiment can be considered to sample a fairly constant energy "tail" of the two final-state protons, accounting for the apparent independence of σ_T and $\bar{x}$ on E_p.

The model assumes that, after a pion is produced, the total energy

available for distribution between the protons and the pion is simply:

$$E_{TOT} = E_p - m_\pi c^2 - E^* \tag{36}$$

where E_p, $m_\pi c^2$ and E^* are the incident proton energy, the pion rest mass and the excitation energy of the nucleus. A normalized probability density, δ, for the two protons to have energies E_1 and E_2 is then defined by:

$$1 = \int_0^{E_{TOT}} \int_0^{E_{TOT}} \delta(E_1, E_2, E_{TOT}) dE_1 \, dE_2 \tag{37}$$

If the probability that a proton of energy E will interact with the nucleus in a way such that no protons (primary or scattered) escape is defined by some function P(E), the relationship between σ_T (where no protons escape) and σ_{inc} (where up to two protons escape) is given by:

$$\frac{\sigma_T}{\sigma_{inc}}(E_p) = \int_0^{E_{TOT}} \int_0^{E_{TOT}} \delta P(E_1) P(E_2) dE_1 \, dE_2 \tag{38}$$

The average energy deposited in the nucleus by the trapped protons is given by:

$$E_{DEP} = \left(\frac{\sigma_{inc}}{\sigma_T}\right) \int_0^{E_{TOT}} \int_0^{E_{TOT}} \delta P(E_1) P(E_2) (E_1 + E_2) dE_1 \, dE_2 \tag{39}$$

Including the initial excitation energy of the pion production step, the total excitation energy of the nucleus is $E_{DEP} + E^*$. The expected average number of evaporated neutrons is simply

$$\bar{x} = \frac{E_{DEP} + E^*}{\langle B_n \rangle + \langle kT \rangle} \qquad (40)$$

where $\langle B_n \rangle$ is the average neutron binding energy and $\langle kT \rangle$ is the smaller kinetic energy. On the assumption that initial pion production occurs in a collision with a nucleon at the top of the Fermi sea, E^* is approximated by $E^* \approx B_n$. In order to obtain quantitative results from Equations 38 through 40, realistic forms of δ and P(E) are required. Kelson treats the three final-state particles as independent and quasi-free, correlated only by total energy conservation in a non-relativistic system. δ is given the form:

$$\delta \propto (E_1 E_2)^{1/2} (E_{TOT} - E_1 - E_2) \qquad (41)$$

The function P(E) can in principle be evaluated from intranuclear cascade types of considerations. However, in the calculation it is represented in a simple one parameter form based indirectly on INC considerations. Below the Coulomb barrier (B) for proton emission, the escape probability is practically zero and

$$P(E) = 1, \text{ for } E < B$$

For energies above the barrier,

$$P(E) = \exp\{-(E-B)/\omega\}, \text{ for } E \geq B$$

The parameter ω is monotonically related to the nucleon mean free path, though the exact relation is not clear. In the calculations, both σ_{inc}/σ_T and $\bar{x}$ are sensitive to the one parameter (ω). Figures 20 and 21

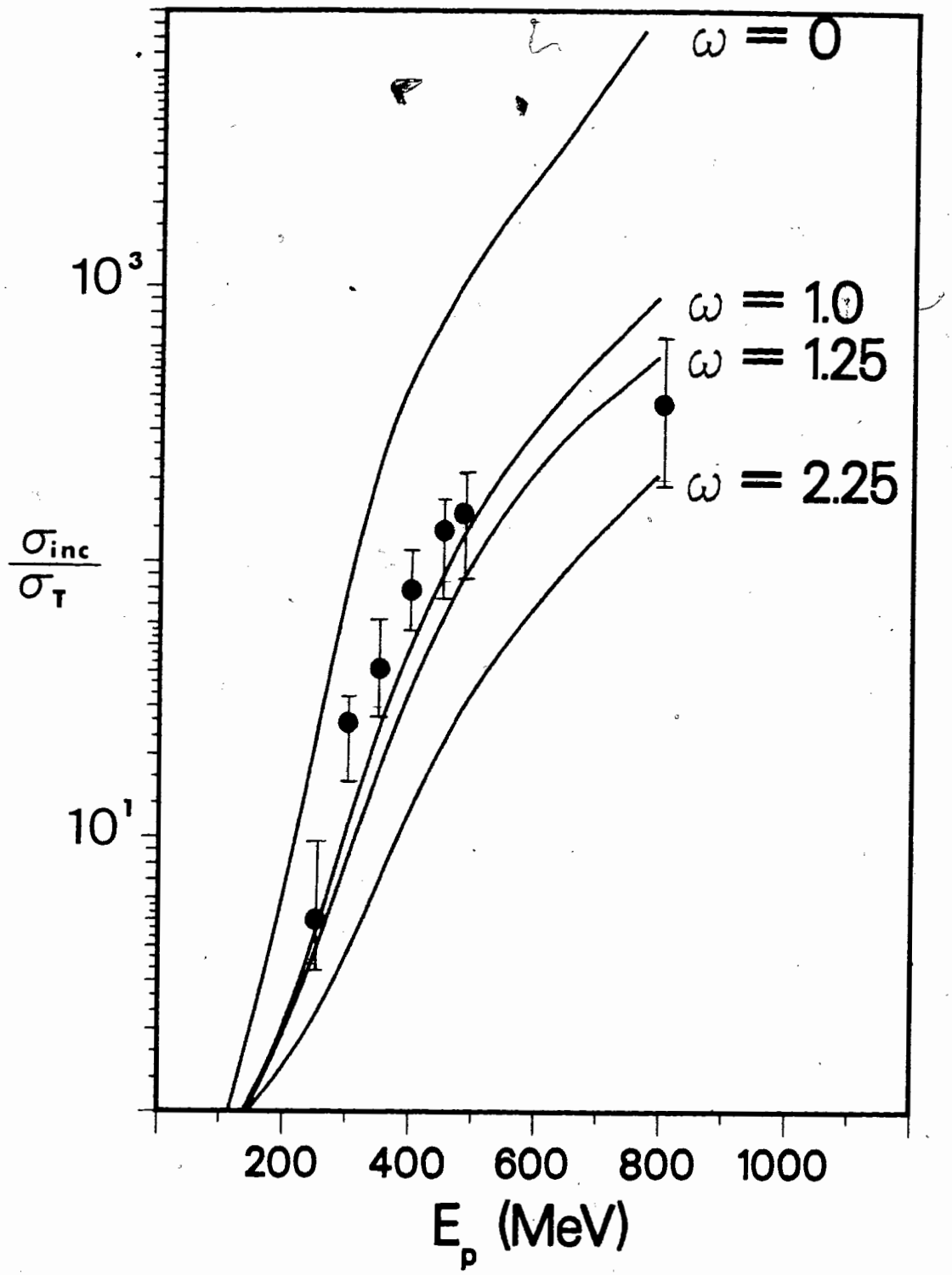

Figure 20 The Ratio σ_{inc}/σ_T as a Function of Proton Energy for a Number of Values of Parameter ω

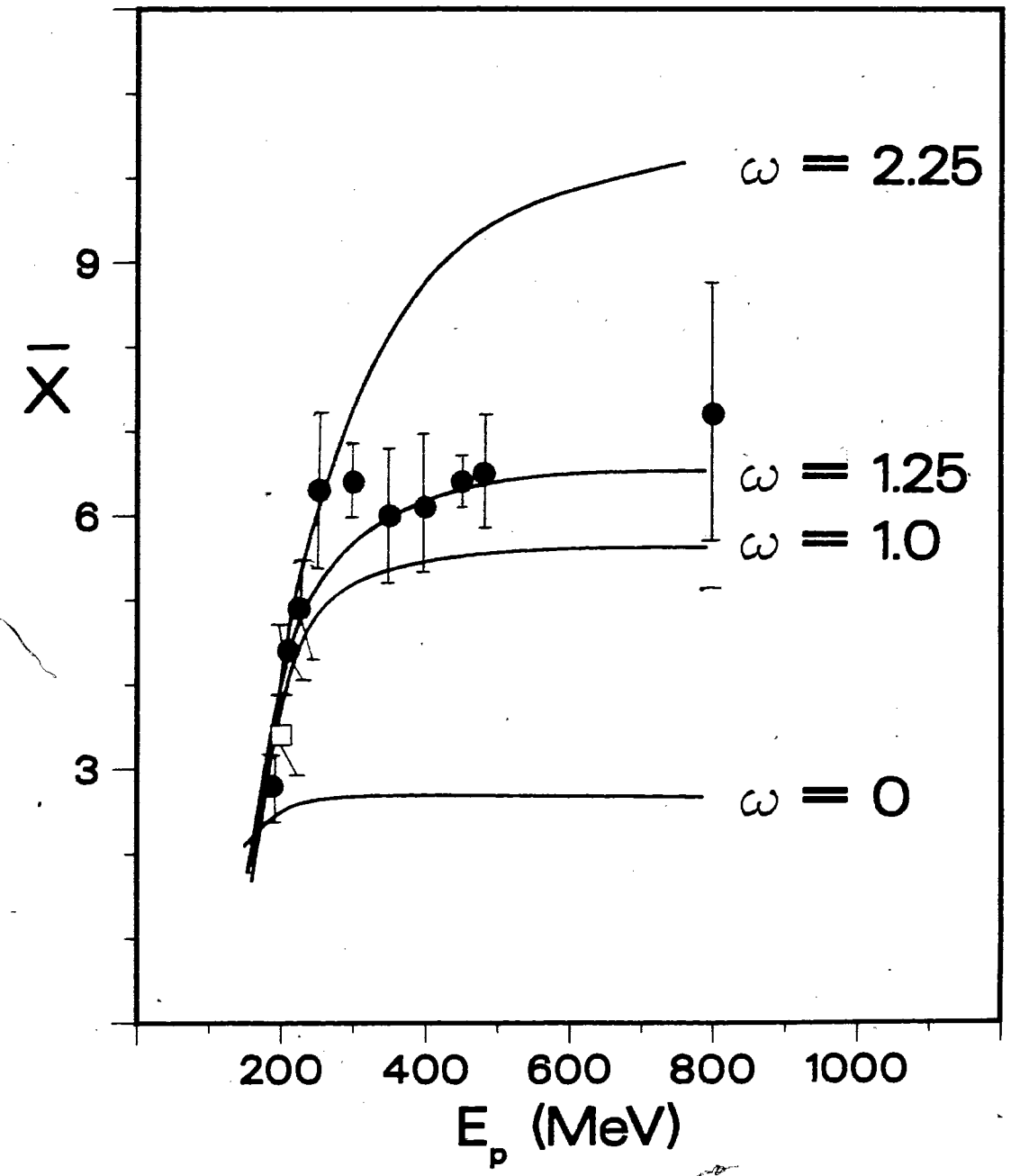

Figure 21 The Value of $\bar{x}$ as a Function of Proton Energy for a Number of Values of Parameter ω

display the results of Kelson's calculations compared with the experimental results. The values of σ_{inc} have been extrapolated from Figure 19. The fact that both quantities are satisfied by the same value of ω lends support to the assumptions of the schematic model.

SUMMARY

The $^{209}Bi(p,\pi^-xn)^{210-x}At$ reactions, with x = 0-7, have been studied in the energy region 120-800 MeV. Though little information was obtained on the coherent $^{209}Bi(p,\pi^-)^{210}At$ reaction, the other excitation functions show an energy dependence similar to that of $^{209}Bi(p,\pi^0)^{210}Po$[19] and of other xn type reactions[57]. The similarity between the excitation functions of the (p,π^0) and (p,π^-xn) reactions as well as the fact that both can be described by two-nucleon mechanisms (by Dillig[19] for (p,π^0) and Gibbs[21] for (p,π^-xn)) suggest that the mechanisms for both π^- and π^0 production in heavy nuclei are similar. Both calculations rely on the population of high-lying final nuclear states. Residual nuclei with 5-7 neutrons removed from the coherent product were found to be favoured in the (p,π^-xn) reaction channel. The residual astatine mass distributions could be fit with a Gaussian shape that implies an average residual excitation energy (≈60 MeV) and momentum transfer (≈335 MeV/c) for the (p,π^-xn) channel. This momentum transfer is similar to that observed for the series of (p,xn)[34] charge exchange reactions and other proton induced reactions at medium energy[60,61] and suggests there is a similar average amount of momentum transfer for reaction channels involving only neutron emission. The measured energy dependence and mass distributions are in good agreement with the two-nucleon mechanism calculation of Gibbs[21] at lower proton energies. While the magnitude of the estimated total cross section in the (p,π^-xn) channel (σ_T) is not reproduced by the two-nucleon calculation, it is possible a minor correction to the assumed level density can account for the discrepancy. The estimated magnitude of σ_T, up to $E_p \approx$ 220 MeV, is in agreement with an intranuclear cascade calculation[22] that

attributes more than half of the pion production to charge exchange processes. At incident energies below ≈250 MeV, the (p,π^-xn) channel dominates the inclusive π^- production. Above 250 MeV, σ_T remains at a relatively constant value accounting for only $\lesssim 0.5\%$ of the inclusive cross section. This low value is not surprising since reaction channels involving charged particle emission become energetically feasible at higher energies and apparently dominate the (p,π) cross section. Over the entire energy region, the energy dependence of σ_T/σ_{inc} and the average number of evaporated neutrons are reproduced well by a schematic model[63] that takes into account the probabilities of one or two proton emission. Although no definite conclusions on the underlying mechanism of (p,π^-xn) reactions can be made, the similar energy dependence of σ_T to σ_{np} (the elementary $np \rightarrow pp\pi^-$ cross section) and the qualitative agreement with the two-nucleon model can support a direct pion production mechanism.

Since σ_T is such a minor component of σ_{inc} at higher energies, it is interesting to ask what reaction (or collection of reactions) is responsible for π^- production at higher energies. It may well be that channels such as $(p,p\pi^-xn)$ or $(p,2p\pi^-xn)$ are dominant. Unfortunately, these reactions cannot be examined by simple radiochemical methods. Much more complex experiments involving coincidence measurements of emitted particles would be required.

REFERENCES

1. D.F. Measday and G.A. Miller, Ann. Rev. Nucl. Part. Sci. 29, 121 (1979).

2. B. Höistad, Adv. Nucl. Phys. 11, 135 (1978).

3. M. Dillig, Nucl. Phys. A335, 407 (1980).

4. H.W. Fearing, TRIUMF Report. No. TRI-80-3 (1980), unpublished.

5. "Pion Production and Absorption in Nuclei", edited by R.D. Bent, AIP Conf. Proc. No. 79 (1981).

6. S.E. Vigdor, T.G. Throwe, H.C. Green, W.W. Jacobs, R.D. Bent, J.J. Kehayias, W.K. Pitts and T.E. Ward, Nucl. Phys. A396, 610 (1983).

7. J.F. Crawford, M. Daum, G.H. Eaton, R. Frosch, H. Hirschmann, R. Horisberger, J.W. McCulloch, E. Steiner, R. Hausmmann, R. Hess and D. Werren, Phys. Rev. C22, 1184 (1980).

8. D.R.F. Cochran, P.N. Dean, P.A.M. Gram, E.A. Knapp, E.R. Martin, D.E. Nagle, R.B. Perkins, W.J. Shlaer, H.A. Thiessen and E.D. Theriot, Phys. Rev. D6, 3085 (1972).

9. N.J. DiGiacomo, M.R. Clover, R.M. DeVries, J.C. Dousse, J.S. Kapustinsky, P.L. McGaughey, W.E. Sondheim, J.W. Sunier, M. Buenerd and D. Lebrun (private communication).

10. V.A. Krasnov, A.B. Kurepin, A.I. Reshetin, K.O. Oganesjan and E.A. Pasyuk, Phys. Lett. 108B, 11 (1982).

11. J. Julien, M. Bolore, X. Charlot, J.M. Hisleur, J. Martino, G.S. Pappalardo, L. Roussel, B. Saghai, G. Sanouillet, L. Bimbot, D. Lebrun, F.F. Guber, A.B. Kurepin and A.I. Reshetin, Phys. Lett. 142B, 340 (1984).

12. S.B. Kaufman and E.P. Steinberg, Phys. Rev. C22, 167 (1980).

13. J. Hudis, in "Nuclear Chemistry", edited by L. Yaffee, Academic Press, New York, Vol. I, p. 169 (1968).

14. S. Sekerskii and A.K. Lavrukhina, Sov. Phys. Doklady Akad. NAUK SSR 117, 61 (1957) (in Russian).

15. A.K. Lavrukhina, I.M. Grechishcheva and B.A. Khotin, J. Atomic Energy (USSR) 6, 142 (1959) (in Russian).

16. L.P. Remsberg, Phys. Rev. 138, B572 (1965).

17. A.M. Poskanzer, J.B. Cumming and L.P. Remsberg, Phys. Rev. 168, 1331 (1968).

18. S. Zauner, J.V. Kretz and E. Kuchinka, GSI Report 84-1, p. 233.

19. T.E. Ward, P.D. Singh, D.L. Friesel, A.I. Yavin, A. Doron, J.M. D'Auria, G. Sheffer and M. Dillig, Phys. Rev. C24, 588 (1981).

20. J.L. Clark, P.E. Haustein, T.J. Ruth, J. Hudis and A.A. Caretto, Jr., Phys. Rev. C27, 1126 (1983).

21. W.R. Gibbs, Ref. 5, p. 297.

22. D.G. Long, M.M. Sternheim and R.R. Silbar, Phys. Rev. C26, 586 (1982).

23. J.B. Cumming, Ann. Rev. Nucl. Sci. 13, 261 (1963).

24. A. Poskanzer, J.B. Cumming and R. Wolfgang, Phys. Rev. 129, 374 (1963).

25. "Table of Isotopes", 7th Ed., edited by C.M. Lederer and V. Shirley, Wiley & Sons, New York (1978).

26. G.L. Johnson, R.F. Leininger and E. Segre, J. Chem. Phys. 17, 1 (1949).

27. A.H.W. Auten, Jr., T. Doorgeest, V. Hollstein and P.H. Moeken, Analyst 77, 774 (1952).

28. G.J. Meyer and K. Rossler, Radiochem. Radioanal. Lett. 25, 377 (1976).

29. E.H. Appelman, "The Radiochemistry of Astatine", U.S. At. Energy Comm., NAS-NS-3012 (1960).

30. G. Barton, Jr., A. Ghiorso and I. Perlman, J. Inorg. Nucl. Chem. 26, 13 (1951).

31. M. Bochvarova, Di Kim Tyung, I. Dudova, Yu.V. Norseev and V.A. Khalkin, Soviet Radiochemistry 14, 889 (1972).

32. T.J. Ruth (private communication).

33. J.L. Clark, Ph.D. thesis, Carnegie-Mellon Univ. (1980).

34. J.M. D'Auria, M. Dombsky, G. Sheffer, T.E. Ward, H.J. Karwowski, A.I. Yavin and J.L. Clark, Phys. Rev. C30, 236 (1984).

35. R. Gunnink and J.B. Niday, Computerized Analysis by γ-Ray Spectrometry, Vol. I-UCRL-51061, Vol. 1 (1972).

36. A.H. Wapstra and K. Bos, Atomic Data and Nucl. Data Tables 19(3), 175 (1977).

37. R.E.L. Green and R.G. Korteling, Phys. Rev. C 22(4), p. 1594 (1980).

38. E.N. Vol'nin, A.A. Vorob'ev and D.M. Seliverstov, Zh. Eksp. Teor. Fiz. Pis'ma RED 19, 691 (1974) [Sov. Phys. JETP Lett. 19, 357 (1974)].

39. B.V. Kurchatov, V.N. Mekhedov, L.V. Chistiakov, M.Ya. Kuznetsova, N.I. Borisova and V.G. Solov'ev, Zh. Eksp. Teor. Fiz. 35, 56 (1958) [Sov. Phys. JETP 35(8), 40 (1959)].

40. Wang Yung-Yü, V.V. Kusnetsov, M.Ya. Kusnetsova and V.A. Khalkin, Zh. Eksp. Teor. Fiz. 39, 230 (1960) [Sov. Phys. JETP 12(2), 166 (1961)].

41. Li Chung Hi, N.S. Mal'tseva and V.N. Mekhedov, Yad. Fiz. 14, 484 (1971) [Sov. J. Nucl. Phys. 14(3), 272 (1972)].

42. M. Lefort, G. Simonoff, X. Tarrago, Nuc. Phys. 19, 173 (1960).

43. H. Gauvin, M. Lefort, X. Tarrago, Nuc. Phys. 39, 447 (1962).

44. M. Lefort and X. Tarrago, Nuc. Phys. 46, 161 (1963).

45. A.E. Metzger and J.M. Miller, Phys. Rev. 113(4), 1125 (1959).

46. J.R. Wu, C.C. Chang and H.D. Holmgren, Phys. Rev. C 19(3), 698 (1979).

47. R.E. Segel, T. Chen, L.L. Rutledge, Jr., J.V. Maher, J. Wiggins, P.P. Singh and P.T. Debevec, Phys. Rev. C 26(6), 2424 (1982).

48. Private communication via J.L. Clark.

49. J.D. Jackson, Can. J. Phys. 34, 767 (1956).

50. E.L. Kelly and E. Segre, Phys. Rev. 75(7), 999 (1949); J.D. Stickler and K.J. Hofstetter, Phys. Rev. C 9(3), 1064 (1974).

51. G. Deconninck and M. Longrée, Annal. de la Soc. Scientifique de Bruxelles 88(3), 347 (1974).

52. W.J. Ramler, J. Wing, D.J. Henderson and J.R. Huizenga, Phys. Rev. 114(1), 154 (1959).

53. M. Lefort, "Nuclear Chemistry", V. Van Nostrand Co. Ltd., London (1968), pp. 207-208.

54. M.M. Shapiro, Phys. Rev. 90(2), 171 (1953).

55. H.A. Bethe, Z. Physik 76, 293 (1932).

56. J.F. Ziegler, Nucl. Instr. Methods 168, 17 (1980).

57. Y. Ohkubo, N.T. Porile, C.J. Orth and L.C. Liu, Phys. Rev. C27, 1146 (1983).

58. J.G. Rushbrooke, D.V. Bugg, A.J. Oxley, J.A. Zoll, M. Jobes, J. Kinson, L. Riddiford and B. Tallini, Nuovo. Cimento 33, 4789 (1964).

59. W.O. Lock and D.F. Measday, "Intermediate Energy Nuclear Physics", Methuen & Co., London (1970).

60. F. Saint Laurent, M. Conjeaud, R. Dayras, S. Harar, H. Oeschler and C. Volont, Phys. Lett. 110B, 372 (1982).

61. L.W. Woo, K. Kwiatkowski and V.E. Viola, Jr., Phys. Lett. 132B, 283 (1983).

62. D.G. Long and M.M. Sternheim, Phys. Rev. C26, 1558 (1982).

63. I. Kelson (private communication).

64. R. Handler, Phys. Rev. 138, B1230 (1965).

65. V.P. Dzhelepov, V.S. Kiselev, K.O. Oganesian and V.B. Fliagin, Soviet Physics JETP 23, 993 (1966).

66. Yu.M. Kazarinov and Yu.N. Simonov, Soviet J. Nucl. Phys. 4, 100 (1967).